ACSNANO

www.acsnano.org

ARTICLE

Photo-Inspired Antibacterial Activity and Wound Healing Acceleration by Hydrogel Embedded with Ag/Ag@AgCl/ZnO Nanostructures

Congyang Mao,[†] Yiming Xiang,[†] Xiangmei Liu,[†] Zhenduo Cui,[‡] Xianjin Yang,[‡] Kelvin Wai Kwok Yeung,[§] Haobo Pan,[∥] Xianbao Wang,[†] Paul K. Chu,[⊥] and Shuilin Wu*[,†,‡]

[†]Hubei Collaborative Innovation Center for Advanced Organic Chemical Materials, Ministry-of-Education Key Laboratory for the Green Preparation and Application of Functional Materials, Hubei Key Laboratory of Polymer Materials, School of Materials Science and Engineering, Hubei University, Wuhan 430062, China

[‡]School of Materials Science and Engineering, Tianjin University, Tianjin 300072, China

[§]Department of Orthopaedics and Traumatology, Li Ka Shing Faculty of Medicine, The University of Hong Kong, Pokfulam 999077, Hong Kong, China

[∥]Center for Human Tissues and Organs Degeneration, Shenzhen Institutes of Advanced Technology, Chinese Academy of Sciences, Shenzhen 518055, China

[⊥]Department of Physics and Department of Materials Science and Engineering, City University of Hong Kong, Tat Chee Avenue, Kowloon 999077, Hong Kong, China

Supporting Information

ABSTRACT: **Ag/Ag@AgCl/ZnO hybrid nanostructures are embedded in a hydrogel by a simple two-step technique. The Ag/Ag@AgCl nanostructures are assembled in the hydrogel *via* ultraviolet light chemical reduction followed by incorporation of ZnO nanostructures by NaOH precipitation. The hydrogel accelerates wound healing and exhibits high antibacterial efficiency against both *Escherichia coli* and *Staphylococcus aureus* under visible light irradiation. The Ag/Ag@AgCl nanostructures enhance the photocatalytic and antibacterial activity of ZnO due to the enhancement of reactive oxygen species by visible light. This hydrogel system kills 95.95% of *E. coli* and 98.49% of *S. aureus* within 20 min upon exposure to simulated visible light, and rapid sterilization plays a crucial role in wound healing. In addition, this system provides controllable, sustained release of silver and zinc ions over a period of 21 days arising from the reversible swelling−shrinking transition of the hydrogel triggered by the changing pH value in the biological environment. About 90% Zn^{2+} release is observed in the acidic environment after 3 days, whereas only 10% Zn^{2+} release occurs in the neutral environment after 21 days. *In vivo* results show that release of Ag^{+} and Zn^{2+} stimulates the immune function to produce a large number of white blood cells and neutrophils (2−4 times more than the control), thereby producing the synergistic antibacterial effects and accelerated wound healing.**

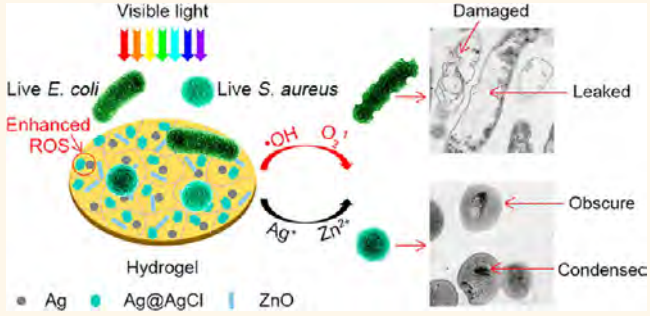

KEYWORDS: *hydrogel, visible light irradiation, antibacterial activity, photodynamic therapy, wound healing*

Serious tissue damage can result from infection caused by microorganisms especially *Staphylococcus aureus* (*S. aureus*)[1−3] and rapid wound treatment has therefore attracted much attention. A moist environment is required for wound healing.[4] Since hydrogels are hydrophilic and environment-friendly polymers with biodegradability and excellent biocompatibility as well as a three-dimensional polymeric network, they are capable of swelling by 10 times in volume after absorbing a large amount of water.[5−11] They can thus be employed as carriers of antimicrobial agents and tissue regenerative materials, that is, hydrogels can absorb ichor and killing bacteria in wounds,[4,12] and there have been efforts to

Received: May 19, 2017
Accepted: August 21, 2017
Published: August 21, 2017

© 2017 American Chemical Society

DOI: 10.1021/acsnano.7b03513
ACS Nano 2017, 11, 9010−9021

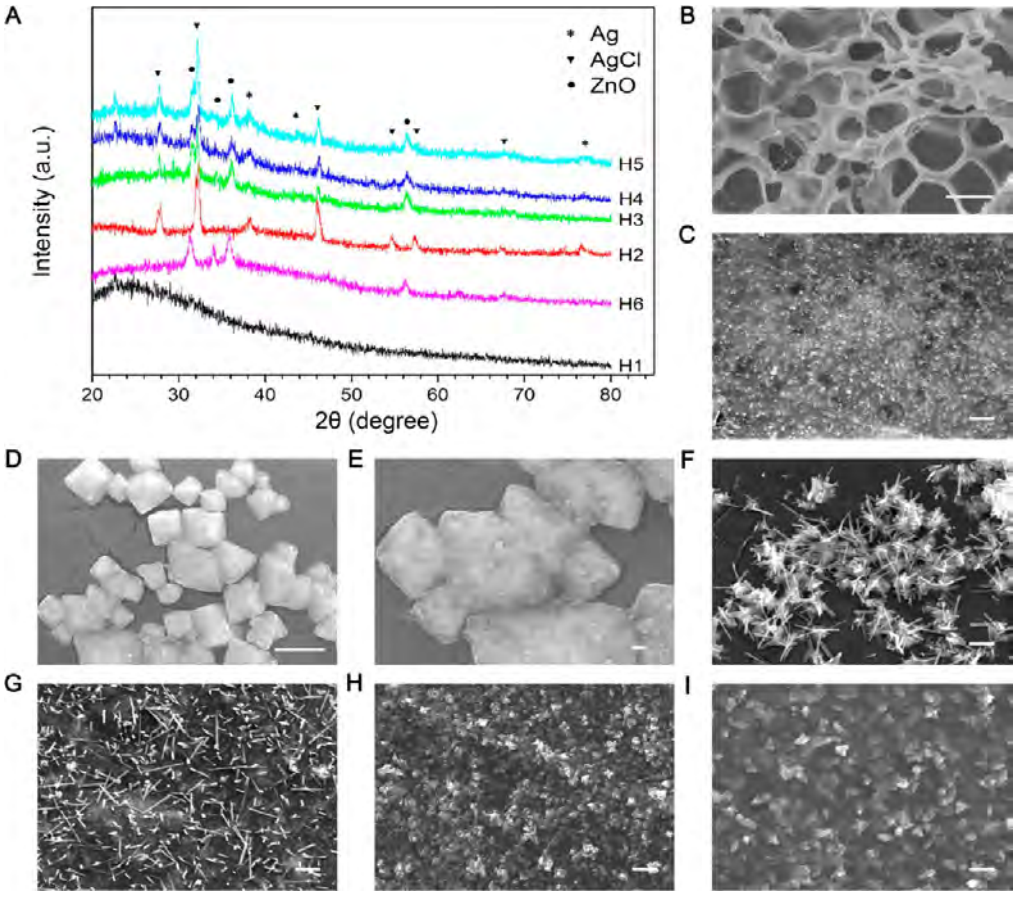

Figure 1. Microstructural and morphological characterization of the hydrogels (H1: control hydrogel; H2: Ag/Ag@AgCl hydrogel; H3, H4, and H5: Ag/Ag@AgCl/ZnO hydrogels with initial $AgNO_3$ concentrations of 0.75, 1.25, and 2.5 mM, respectively; H6: ZnO hydrogel). (A) XRD patterns of the hydrogels. (B) SEM image of the representative networks of hydrogel in H1. Scale bar, 10 μm. (C) SEM image of highly dispersed Ag NPs in H2 derived from the chemical reduction of $AgNO_3$ by ultraviolet light. Scale bar, 1 μm. (D) SEM image of the typical cube-like nanostructured Ag@AgCl. Scale bar, 1 μm. (E) The magnified SEM image of Ag@AgCl. Scale bar, 100 nm. SEM images of ZnO nanospecies with different morphologies in H3 (F), H4 (G), H5 (H), and H6 (I), respectively, derived from the precipitation of $Zn(NO_3)_2$ in NaOH solution. Scale bars, 1 μm.

modify hydrogels with antibacterial agents such as inorganic antimicrobial agents including Ag nanoparticles (NPs), ZnO NPs, and graphene as well as organic antimicrobial agents like ciprofloxacin, vancomycin, and chloramphenicol.[13−19] However, inorganic antimicrobial agents commonly exhibit some cytotoxicity[20,21] and organic agents are sometimes unstable and drug resistant because of widespread antibiotic abuse.[22−24]

Semiconductor nanostructures such as ZnO are widely used in solar energy conversion, antimicrobial agents, and photocatalysis for degradation of environmental pollutants.[25−28] The energy created by charge separation and electron−hole pairs during light exposure has many important applications.[29−31] Reactive oxygen species (ROS) such as singlet oxygen, hydroxyl radicals, and superoxide radicals have been reported as the main reactive species in the photocatalytic activity of semiconductor nanomaterials[32,33] and also have excellent antibacterial properties.[29,34] Additionally, Zn^{2+} released from ZnO can promote production of fibroblasts that are particularly important to proliferation and differentiation into myofibroblasts in the dermis and subcutaneous tissues surrounding wounds during skin regeneration.[35−39] However, pure ZnO nanomaterials usually exhibit relatively low photoenergy conversion efficiency due to the low charge separation efficiency and the rapid recombination of charge carriers.[29]

Recently, a visible light-triggered, highly efficient, stable photocatalyst active system composed of Ag@AgCl has been proposed.[40−43] Silver halide which has been used extensively in photographic films as photosensitive materials[44,45] generates electron−hole pairs after light absorption, and Ag atoms are created by the combination of Ag^+ and photogenerated electrons. Compared to pure ZnO, ZnO incorporated with Ag NPs exhibits enhanced antimicrobial activity because an appropriate amount of Ag can enhance the photocatalytic activity related to the antimicrobial activity.[22] However, visible light-inspired and environmentally benign hybrid materials which not only produce highly effective antibacterial activity through ROS generation by enhanced photocatalytic properties and accelerate wound healing have not been reported.

Moreover, carboxymethyl cellulose (CMC) is a natural occurring polysaccharide, which is toxicologically innocuous with good solubility and high chemical stability, thereby making it a suitable biomaterial for the preparation of the hydrogel.[46,47] Herein, we describe a hydrogel composite incorporated with CMC and Ag/Ag@AgCl/ZnO hybrid nanostructures that exhibits excellent photocatalytic activity and broad antibacterial efficiency against both Gram-positive and Gram-negative bacteria under visible light irradiation. This reversible swelling−shrinking transition is triggered by changing pH in

DOI: 10.1021/acsnano.7b03513
ACS Nano 2017, 11, 9010−9021

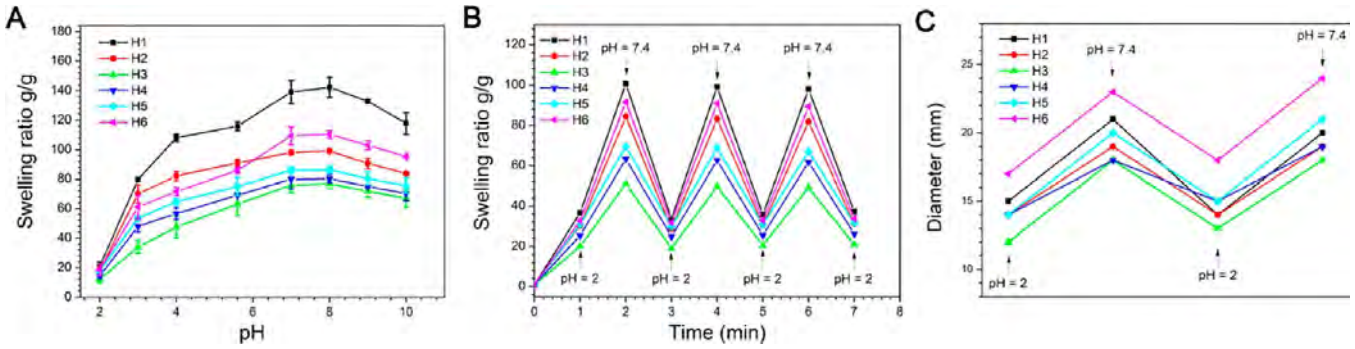

Figure 2. Swelling behavior of the hydrogels (H1: control hydrogel; H2: Ag/Ag@AgCl hydrogel; H3, H4, and H5: Ag/Ag@AgCl/ZnO hydrogels; H6: ZnO hydrogel). (A) Swelling curves of the hydrogels after immersed in aqueous solutions with set pH values of 2, 3, 4, 5.6, 7, 8, 9, and 10 at room temperature for 24 h. The experiment was performed in triplicate and independently (n = 3), and data are mean ± SD. (B) Changes of swelling ratios. (C) Corresponding changes of diameters of hydrogels with 1 min time intervals between the pH changes from 2 to 7.4.

the environment, and this hybrid system could boost the immune system and accelerate wound healing.

RESULTS AND DISCUSSION

Synthesis and Characterization of the Ag/Ag@AgCl/ZnO Nanocomposite Hydrogel. To obtain the Ag/Ag@AgCl/ZnO nanocomposite hydrogel, the CMC hydrogel is allowed to swell by water absorption to open the pores in the gel, as shown in Figure S1. Figure 1A represents the H1, H2, H3, H4, H5, and H6 X-ray diffraction (XRD) patterns. For H1, a wide peak appears at around 23° attributed to the existence of the polymer networks in the CMC hydrogel.[48] After Ag/Ag@AgCl/ZnO doping, this peak weakens and even disappears due to partial destruction of the polymer network by UV light and the basic agent during the NP synthesis process, as shown in Figure S2 (red arrows). With regard to the nanocomposite hydrogels, the reduced Ag NPs are evidenced by the peaks at 2θ = 38.1°, 44.2°, and 77.5° which can be indexed to the (1 1 1), (2 0 0) and (3 1 1) planes of metallic Ag, respectively (JCPDS no. 04-0783)[16] and the diffraction peaks (2θ) at 27.7°, 32.1°, 46.2°, 54.7°, 57.4°, and 67.4° correspond to the (1 1 1), (2 0 0), (2 2 0), (3 1 1), (2 2 2), and (4 0 0) planes of the typical cubic phase of AgCl, respectively (JCPDS no. 31-1238).[42] The precipitated ZnO is indicted by the peaks at 2θ = 31.8°, 34.4°, 36.2°, and 56.6° indexed to the (1 0 0), (0 0 2), (1 0 1), and (1 1 0) planes of the ZnO zincite phase, respectively (JCPDS no. 36-1451).[29]

As shown in Figure 1B, pure CMC hydrogel (H1) has a macroporous sponge-like structure, and the diameter of most pores is about 10 μm. After doping with Ag NPs and Ag@AgCl particles, the Ag NPs are confirmed by the XRD patterns in Figure 1A and uniformly distributed in the samples (H2, Figure 1C), as indicated by the Ag elemental area scan by energy dispersive X-ray spectrometry (EDS) (Figure S3) and transmission electron microscopy (TEM) performed on H2 (Figure S4A). As shown in Figure S4A, 20−40 nm Ag NPs are incorporated into the hydrogel uniformly, and selected area electron diffraction (SAED) confirms the existence of metallic Ag^0 (inset in Figure S4A) and typical cube-like nanostructured Ag@AgCl with a size of about 600 nm (Figure 1D). As shown in Figure 1E, the magnified scanning electron microscopy (SEM) image of the cube-like nanostructures shows that the Ag NPs grow on the surface of the cube-like nanostructures, and it is corroborated by the EDS spectra acquired from the cube-like Ag@AgCl nanostructures (Figure S5). The cube-like nanostructures are composed of Ag and Cl with the former being the majority implying the existence of metallic Ag^0. Following ZnO doping, one-dimensional ZnO nanostructures are produced. In H3 and H4, ZnO has the typical nanorod morphology and aggregates in the substrate of the former (Figure 1F) and is distributed evenly in the latter (Figure 1G). When the content of $AgNO_3$ is increased to 2.5 mM, no obvious ZnO nanorods can be observed, and the high-magnification images show irregular ZnO NPs with a uniform distribution in the substrate (H5, Figure 1H). It is believed that the good lattice and symmetry matching between the ZnO and Ag and direct interface between the Zn layer and Ag initiate the formation of the ZnO lattice, resulting in the growth of the ZnO nanorods.[49,50] To confirm the existence of metallic Ag^0 species in the ZnO nanorods, TEM is performed (Figure S4B). Some of the Ag NPs are attached to the ZnO nanorods in the hydrogel, and SAED confirms the existence of metallic Ag^0 (Figure S4B inset). After ZnO doping without Ag NPs as a precursor, the one-dimensional nano ZnO phase is uniformly distributed in the hydrogel substrate (H6, Figure 1I), and a single ZnO NP is indicated in Figure S4C and can also be determined by SAED (Figure S4C inset). The macroporous sponge-like structures are further demonstrated in Figure S6.

Swelling Behavior. Swelling is one of the important properties of hydrogels. In order to study the dependence on pH, the swelling behavior is investigated at different pH values from 2 to 10. As shown in Figure 2A, the swelling ratios of the hydrogels increase as the pH is raised from 2 to 8 but decrease when the pH is higher than 8. A detailed description of the swelling behavior is provided shown in the Supporting Information.

The reversible swelling−shrinking behavior of the hydrogels is studied in solutions at intervals of 1 min as the pH is changed from 2 to 7.4. As shown in Figure 2B, when the pH is 7.4, the electrostatic repulsive force causes swelling, but shrinking occurs within 1 min due to protonation of the carboxylate groups when the pH is 2. Hence, the hydrogels are sensitive to pH. They have a larger diameter in the neutral environment than in the acidic environment, as shown in Figure 2C.

Silver and Zinc Ion Release and Antibacterial Activity *in Vitro*. Figure 3A,B shows the cumulative Ag^+ (H2, H3, H4, and H5) released from the nanocomposite hydrogels in the phosphate-buffered saline (PBS) at pH of 7.4 and 5.6, respectively. An initial burst release is observed in the first 3 days, followed by a slower release from all the hydrogels. H2

DOI: 10.1021/acsnano.7b03513
ACS Nano 2017, 11, 9010−9021

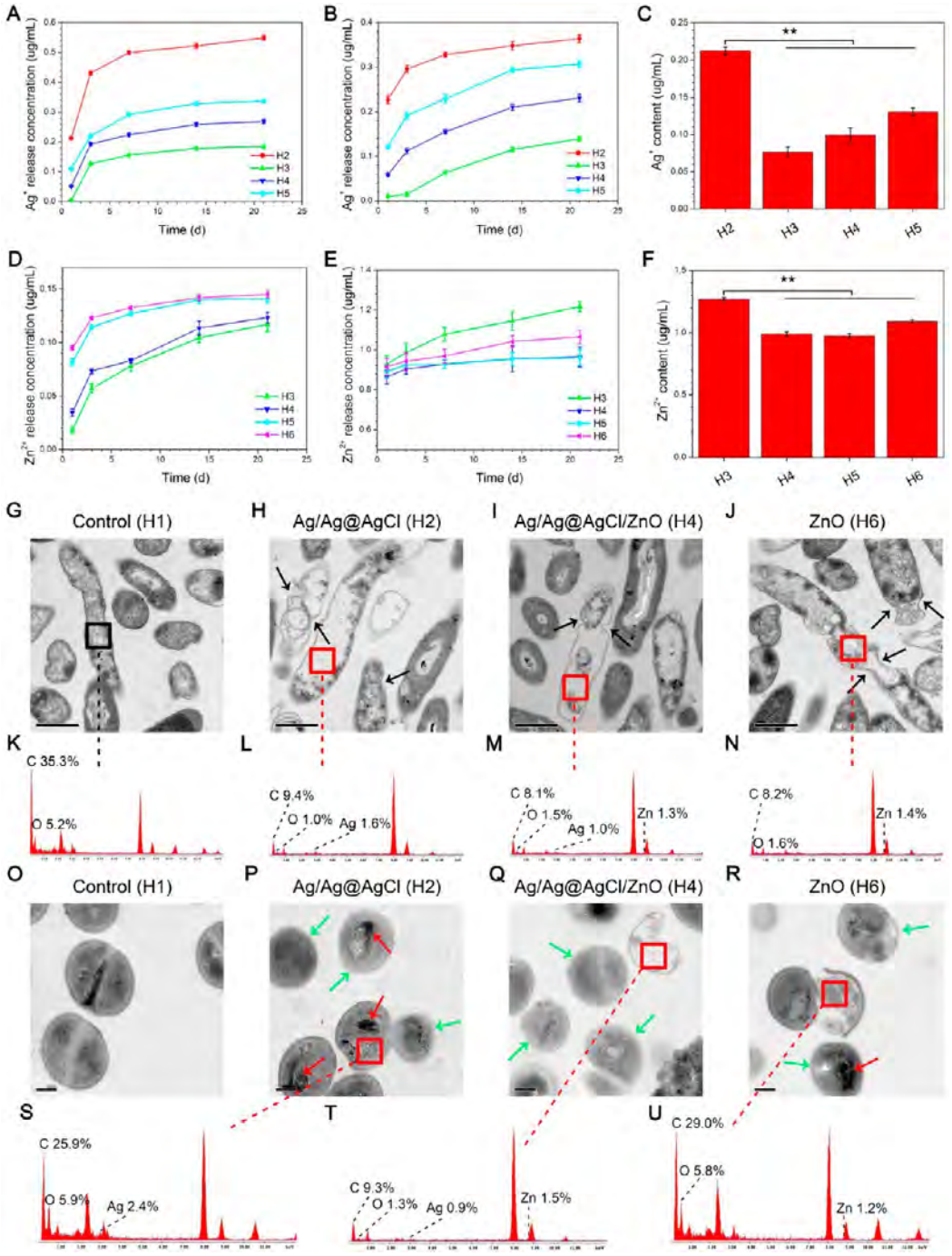

Figure 3. Silver and zinc ion release properties and evaluation of the antibacterial activity *in vitro*. (H1: control hydrogel; H2: Ag/Ag@AgCl hydrogel; H3, H4, and H5: Ag/Ag@AgCl/ZnO hydrogels, and H4 for representative; H6: ZnO hydrogel). Cumulative silver ions release profiles from the argentiferous hydrogels (H2, H3, H4, and H5) in pH 7.4 (A) and 5.6 (B) PBS at days 1, 3, 7, 14, and 21. The experiment was performed in triplicate and independently (n = 3), and data are mean ± SD. The contents of silver (C) of the corresponding hydrogels nitrified by concentrated nitric acid (n = 3, mean ± SD.). Cumulative zinc ions release profiles from the zinciferous hydrogels (H3, H4, H5, and H6) in pH 7.4 (D) and 5.6 (E) PBS at days 1, 3, 7, 14, and 21 (n = 3, mean ± SD) and the contents of zinc (F) of the corresponding hydrogels nitrified by concentrated nitric acid (n = 3, mean ± SD). TEM images of *E. coli* sections after treated with control hydrogel (G, H1), Ag/Ag@AgCl hydrogel (H, H2), the representative Ag/Ag@AgCl/ZnO hydrogel (I, H4), and ZnO hydrogel (J, H6) for 24 h and prepared with a microtome. Scale bars, 1 μm. The corresponding EDS analysis of square areas in TEM images of *E. coli* sections after treated with H1 (K), H2 (L), H4 (M), and H6 (N). TEM images of *S. aureus* sections after treated with H1 (O), H2 (P), H4 (Q), and H6 (R) for 24 h and prepared with a microtome. Scale bars, 200 nm. The corresponding EDS analysis of square areas in TEM images of *S. aureus* sections after treated with H2 (S), H4 (T), and H6 (U).

shows the largest release of Ag^+, whereas H3 has the smallest value, consistent with the initial $AgNO_3$ content in each group as shown in Table S1 (2.5 mM for H2 and H5; 0.75 mM for H3; 1.25 mM for H4). The release from H5 which contains the same initial $AgNO_3$ content as H2 is less than that of H2 due to partial release of Ag NPs and Ag^+ in advance when H5 is

DOI: 10.1021/acsnano.7b03513
ACS Nano 2017, 11, 9010−9021

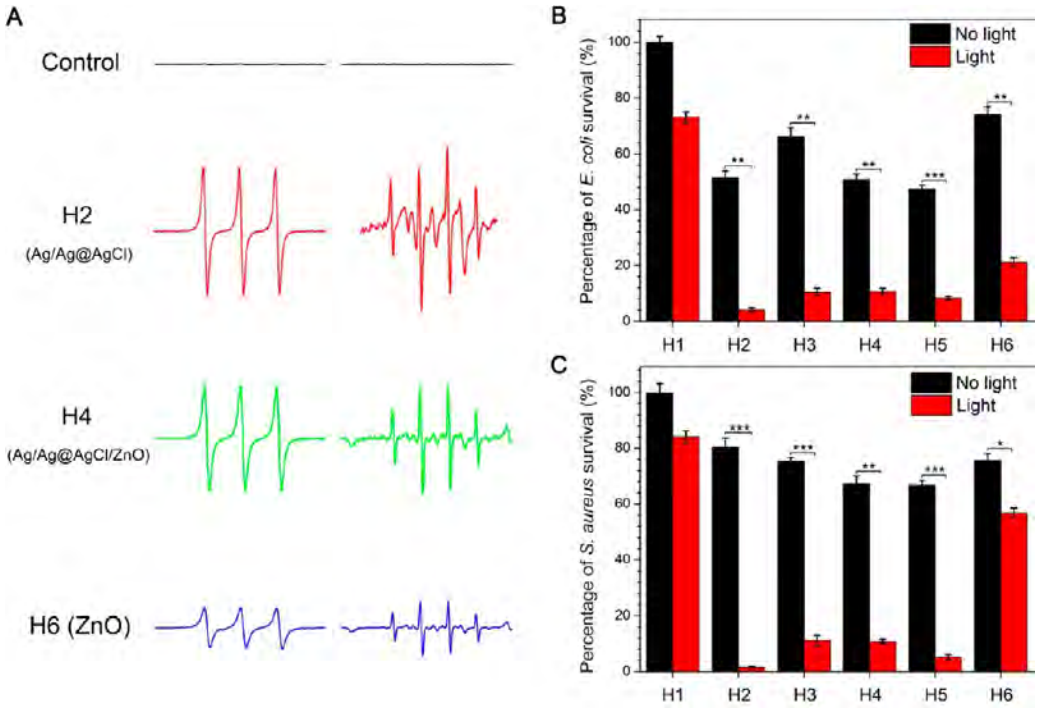

Figure 4. Identification of ROS was detected by ESR spectroscopy and significant enhancement effect on antibacterial activities. (H1: control hydrogel; H2: Ag/Ag@AgCl hydrogel; H3, H4, and H5: Ag/Ag@AgCl/ZnO hydrogels, and H4 for representative; H6: ZnO hydrogel). (A) The ESR spectra of three lines with the intensities of 1:1:1 (left, singlet oxygen (O_2^1) induced by Ag/Ag@AgCl, Ag/Ag@AgCl/ZnO, and ZnO and trapped by TEMP) and four lines with the intensities of 1:2:2:1 (right, hydroxyl radical (•OH) induced by Ag/Ag@AgCl, Ag/Ag@AgCl/ZnO, and ZnO and trapped by DMPO) after irradiated solutions containing the spin traps with simulated sunlight for 5 min. Ability of the hydrogels in killing *E. coli* (B) and *S. aureus* (C) under simulated sunlight for 20 min; the control was in the presence of H1 but in the absence of simulated sunlight. The experiment was performed in triplicate and independently (n = 3), and data are mean ± SD.

immersed in the $Zn(NO_3)_2$ and NaOH solutions. Generally, release of Ag ions from Ag NPs is faster at lower pH (eqs 1 and 2).[52] However, a slower release is observed at a lower pH except in the first day in this case, as shown in Figure S9, and it may be caused by AgCl. In the first day, there is more H^+ in the solution at a lower pH, and Ag NPs dissolve faster producing more Ag^+. Decomposition of AgCl shown in eq 3 creates a steady stream of Ag and results in continuous and slow release of Ag^+ over a long period of time. However, excessive H^+ inhibits dissolution of Cl_2 generated by the decomposition of AgCl in water due to the solubility equilibrium of Cl_2 as described in eq 4. In turn, similar to the butterfly effect, this inhibits decomposition of AgCl as shown in the eq 3, thus blocking the supply of Ag. Therefore, slower release is observed with time at low pH. Because of decomposition of AgCl, the content of Ag^+ at the end of release is larger than that of the initial amount in the samples according to Figure 3A–C.

$$4Ag + O_2 \rightarrow 2Ag_2O \quad (1)$$

$$2Ag_2O + 4H^+ \rightarrow 4Ag^+ + 2H_2O \quad (2)$$

$$2AgCl \rightarrow 2Ag + Cl_2 \quad (3)$$

$$Cl_2 + 2H_2O \rightarrow HOCl + H^+ + Cl^- \quad (4)$$

Figure 3D,E shows the cumulative Zn^{2+} (H3, H4, H5, and H6) released from the nanocomposite hydrogels in PBS at pH of 7.4 and 5.6, respectively. As shown in Figure 3D, the release trend of Zn^{2+} is similar to that of Ag^+. H3 and H4 show nearly the same Zn^{2+} release behavior, and the same trend is observed from H5 and H6 because ZnO has the same nanorod structure in the former two and the same irregular NPs in the latter two. The only difference is the slightly larger Zn^{2+} concentration in H4 than H3 and in H6 than H5 because the distribution of ZnO nanorods in H4 is more uniform than that in H3, thus resulting in a larger surface area of ZnO and more dissolution in the PBS. Hence, both the shape and distribution of ZnO in the substrate influenced the release behavior of Zn^{2+} in the neutral environment. The final Zn^{2+} release quantities in the neutral PBS (Figure 3D) are only about 10% of those loaded originally into the corresponding samples at the pH of 5.6 (Figure 3E). However, in the acidic environment, the only influence of the release behavior of Zn^{2+} is the amount of loaded ZnO because ZnO is extremely unstable in the presence of H^+ and Zn^{2+} as shown in eq 5:[53]

$$ZnO + 2H^+ \rightarrow Zn^{2+} + H_2O \quad (5)$$

As shown in Figure 3E, all the samples show a rapid Zn^{2+} release, and the final Zn^{2+} release quantities are close to loaded amounts in the corresponding samples (Figure 3F). Moreover, the dimensions of ZnO may have an effect on the release of Zn^{2+} and the corresponding biological functions.[51]

The antibacterial activity of the hydrogels against two different bacterial strains, *E. coli* and *S. aureus*, which are responsible for most infections is investigated.[2] As shown in Figure S10A, no inhibition zone is observed from H1 without NPs, whereas clear inhibition zones are formed around the nanocomposite hydrogels. The bacterial growth is determined by the optical density (OD) at 600 nm, and the samples exhibit obvious antibacterial effects in the presence of the nano species (Figure S10B). Both Ag^+ released from the Ag NPs and Zn^{2+}

DOI: 10.1021/acsnano.7b03513
ACS Nano 2017, 11, 9010–9021

released from the ZnO nanostructures are responsible for the antibacterial behavior.[22,52] H2 (highest release of Ag^+) and H3 (highest release of Zn^{2+}) show the best antibacterial effects to *E. coli* and *S. aureus*, respectively. To understand the antibacterial activity of Ag^+ and Zn^{2+}, the cell wall and membrane damage as well as the intracellular structural change in *E. coli* and *S. aureus* are examined by TEM and EDS. As shown in Figure 3G,O, both the *S. aureus* and *E. coli* cells have the normal morphology with distinct cell walls and compact intracellular substrates in the absence of NPs (H1). However, the nanostructure-incorporated samples of both *S. aureus* and *E. coli* show different degrees of distortion. As shown in Figure 3H–J, the cell walls of *E. coli* appear to be damaged and disorganized (black arrows), and the intracellular densities decrease with a large electron-light area around it (red rectangles in Figure 3H–J). EDS (Figure 3L–N) shows a sharp drop in the contents of carbon and oxygen (main components of intracellular substrates,[54,55] 35.3% as shown in Figure 3K reduced to about 8% for carbon and 5.2% reduced to about 1% for oxygen) in these areas, compared to the compact intracellular substrate areas (black rectangles in Figure 3G), revealing that some intracellular substrates are lost. Meanwhile, the edge of the cell walls becomes obscure (green arrows in Figure 3P–R). Some condensed components are observed (red arrows in Figure 3P,Q) for *S. aureus*, and significant intracellular substrate leakage is observed due to damage of the cell wall (Ag/Ag@AgCl/ZnO group marked by the red rectangle in Figure 3Q). In addition, Ag and Zn were detected internally from the corresponding above bacteria (red rectangles in Figure 3P–R) by EDS (Figure 3S–U). It is suspected that the intracellular substrates leak for *E. coli* and that of condensed for *S. aureus* results from penetration of Ag^+ and Zn^{2+} into the bacteria.

The morphology and membrane integrity of the bacteria on the hydrogels are examined by SEM. Figures S11 and S12 show the morphology of *E. coli* and *S. aureus* attached to the surface, respectively. Only a small amount of bacteria adheres to the surface of the nanocomposite hydrogels compared to the untreated hydrogel, indicating that the nanocomposite hydrogels inhibit bacteria adherence, which is crucial to the prevention of biofilm formation. Typically, distorted and wrinkled membranes of *E. coli* (red arrows in Figure S11) and lesions and holes in *S. aureus* (red arrows in Figure S12) are observed. The typical morphology of *E. coli* and *S. aureus* with a smooth surface and rod shape and spherical shape, respectively, is observed on H1 (Figures S11A and S12A), as consistent with TEM.

Figure 4A shows the electron spin resonance (ESR) spectra obtained from the irradiated solutions containing the spin traps. 2,2,6,6-Tetramethylpiperidine (TEMP) is used to detect singlet oxygen (O_2^1) induced by Ag/Ag@AgCl, Ag/Ag@AgCl/ZnO, and ZnO. The control (without samples or with H1) was ESR silent. After irradiation for 5 min, the typical ESR spectra with three lines of relative intensities of 1:1:1 are observed.[29] They are characteristic of the adduct formed between TEMP and singlet oxygen. For the same amount and recording time, the ESR relative intensity generated from the Ag/Ag@AgCl/ZnO nanocomposite hydrogel is significantly higher than that of the pure ZnO nanocomposite hydrogel, indicating that deposition of Ag/Ag@AgCl generates more singlet oxygen. H2 (Ag/Ag@AgCl hydrogel with the largest initial $AgNO_3$ concentration) exhibits the largest ESR signal, indicating that the Ag/Ag@AgCl nanostructures play key roles in enhancing the photogeneration of singlet oxygen. In addition to singlet oxygen, hydroxyl radical is another important ROS. 5,5-Dimethyl-1-pyrroline-*N*-oxide (DMPO) is selected to investigate the effects of the Ag/Ag@AgCl nanostructures on generation of hydroxyl radicals. Similarly, no ESR signal is observed from the control, but an ESR spectrum showing four lines (1:2:2:1)[56] characteristic of the reaction between DMPO and hydroxyl radical is observed. After addition of the Ag/Ag@AgCl nanostructures, the ESR signal increases significantly, and H2 (Ag/Ag@AgCl hydrogel with the largest initial $AgNO_3$ concentration) also shows the largest ESR signal, suggesting that the hydroxyl radical is generated by Ag/Ag@AgCl and ZnO during light irradiation and deposition of Ag/Ag@AgCl boosts photogeneration of the hydroxyl radical.

The antibacterial activity increases significantly after the hydrogels are co-cultured with bacterial strains, irradiated with simulated sunlight for 20 min, and incubated at 37 °C in darkness for 1 h. As shown in Figure S13, both *E. coli* and *S. aureus* grow well in the absence of nano species and irradiation (no light for H1), whereas a small decrease in bacterial survival occurs after irradiating H1 with simulated sunlight (light for H1). The bacteria without any hydrogel are also reduced by 6.68% after irradiation, as shown in Figure S14, and it may be attributed to the small amount of ultraviolet light in the simulated sunlight. The bacteria exposed to the nanocomposite hydrogels without irradiation show decreased survival as shown in Figure 4B,C perhaps due to release of antibacterial ions (Ag^+ and Zn^{2+}) in the co-culturing process. After introducing ZnO, the survival of both *S. aureus* and *E. coli* diminishes further after exposure to simulated sunlight for 20 min, possibly due to ROS generation during photoexcitation of ZnO. The antibacterial activity on the Ag/Ag@AgCl and Ag/Ag@AgCl/ZnO hybrid nanostructures after remaining in darkness for 1 h or irradiation with simulated sunlight for 20 min is enhanced (Figure S15), although the Ag/Ag@AgCl hybrid nanostructures show smaller antibacterial ratios of 91.44% and 71.53% against *E. coli* and *S. aureus* without light, respectively (Figure S10B). In comparison, H2 (Ag/Ag@AgCl hybrid nanostructures) kills bacteria more effectively and quickly (95.95% for *E. coli* and 98.49% for *S. aureus*) within 20 min (1 h in darkness), demonstrating the excellent photocatalytic properties. The dominant mechanism appears to be the enhanced generation of ROS as suggested by the ESR results.

***In Vivo* Assessment of Wound Healing.** The cytocompatibility results *in vitro* are shown in Figure S18. The nanocomposite hydrogels exhibit some cytotoxicity compared to the untreated hydrogel. The cell viability of H6 with ZnO only is reduced to about 20% after 1 day due to the small amount of zinc release, as shown in Figure 3D. The cytotoxicity of zinc depends on the concentration because excessive zinc can introduce cytotoxicity.[57] As a result of release of Zn^{2+}, the cell viability of H6 decreases after 3 and 7 days. It is also observed that the Ag NPs exhibit cytotoxicity at only small concentrations, which cause the cell viability of H2, H3, H4, and H5 with Ag to decrease more than that of H6 after 1 day. However, the Ag/Ag@AgCl/ZnO nanocomposite hydrogels of H3, H4, and H5, especially H4, show lower cytotoxicity than H2 due to the presence of ZnO which reduces the cytotoxicity.

The therapeutic efficacy pertaining to wound healing for the different hydrogels is evaluated using animal models. Four wounds are made and divided into four groups: control group (H1, group I), Ag/Ag@AgCl group (H2, group II), Ag/Ag@AgCl/ZnO group (H4, group III), and pure ZnO group (H6,

DOI: 10.1021/acsnano.7b03513
ACS Nano 2017, 11, 9010–9021

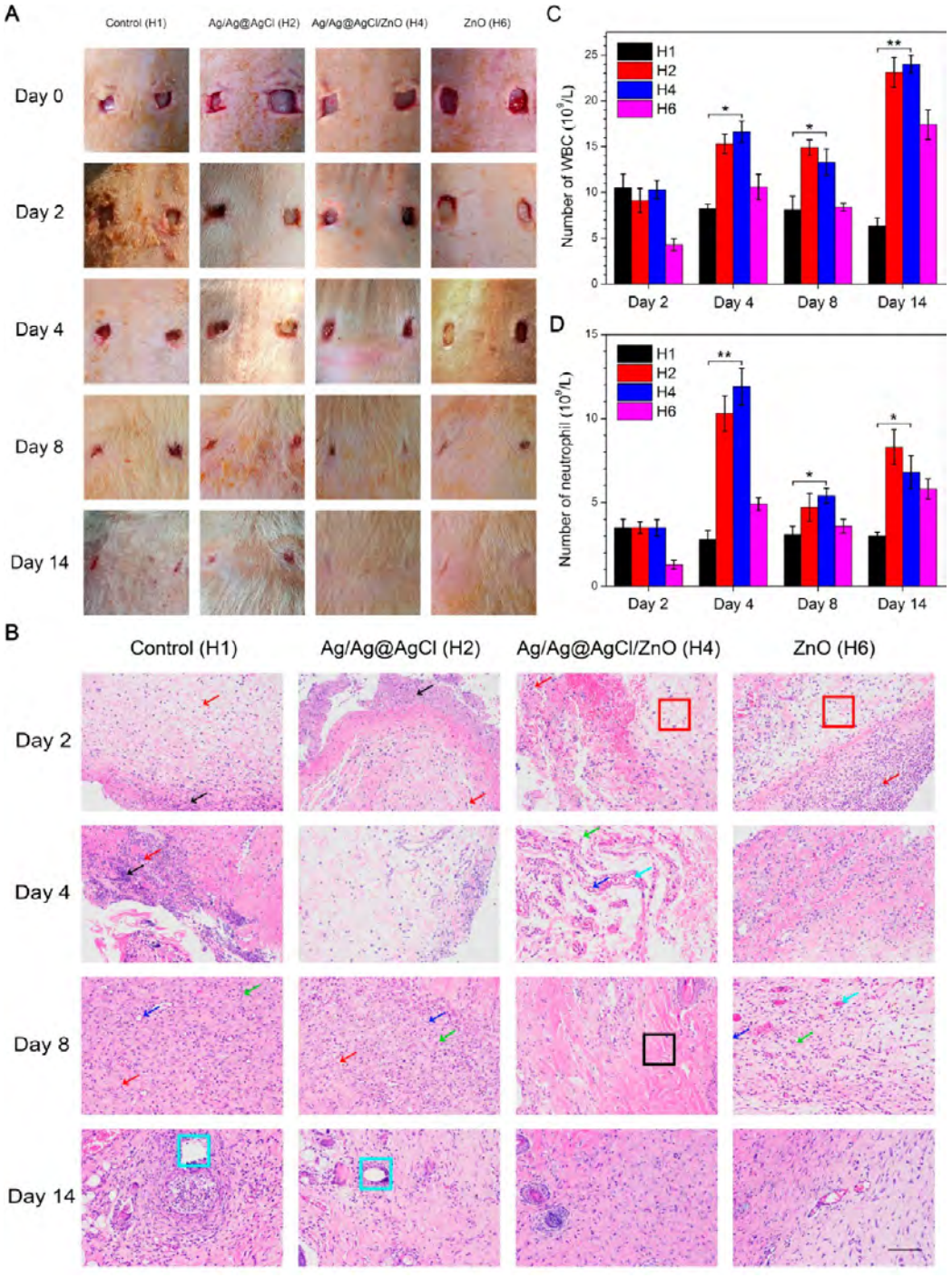

Figure 5. ***In vivo*** **assessments of the hydrogels for wound healing. (H1: control hydrogel; H2: Ag/Ag@AgCl hydrogel; H4: the representative Ag/Ag@AgCl/ZnO hydrogel; H6: ZnO hydrogel). (A)** ***In vivo*** **study on the effects of treatment of** ***S. aureus*****-induced wound infections by hydrogels and the corresponding wound photographs of the rats at days 0, 2, 4, 8, and 14. (B) The immunology of histological images of the skin tissue samples on rats' wounds after treating with hydrogels for 2, 4, 8, and 14 days and staining with H&E. Scale bar, 100 μm.** ***In vivo*** **routine analysis of blood of the numbers of white blood cells (C) and neutrophils (D) in the whole blood extracted from the rats after treating with hydrogels for 2, 4, 8, and 14 days. The experiment was performed in triplicate and independently (n = 3), and data are mean ± SD.**

group IV). The traumas are photographed on days 2, 4, 8, and 14. As shown in Figure 5A, all the groups show severe bacterial infection with ichor after a 2-day treatment. It is consistent with that many viable colony units of *S. aureus* are formed from the exudate of the wounds after the 2-day treatment, as shown in Figure S19. Groups II, III, and IV show a smaller trauma size than the control group after the 8-day treatment, especially the Ag/Ag@AgCl/ZnO group. As shown in Figure S19, the Ag/Ag@AgCl/ZnO group shows better antibacterial effects than the other groups after the 4-day treatment, and few viable colony units are formed after the 8-day treatment. After the 14-day treatment, the wounds of the control and Ag/Ag@AgCl groups do not heal well but those of the groups with ZnO, that is, both Ag/Ag@AgCl/ZnO and pure ZnO groups, show significant healing.

DOI: 10.1021/acsnano.7b03513
ACS Nano 2017, 11, 9010–9021

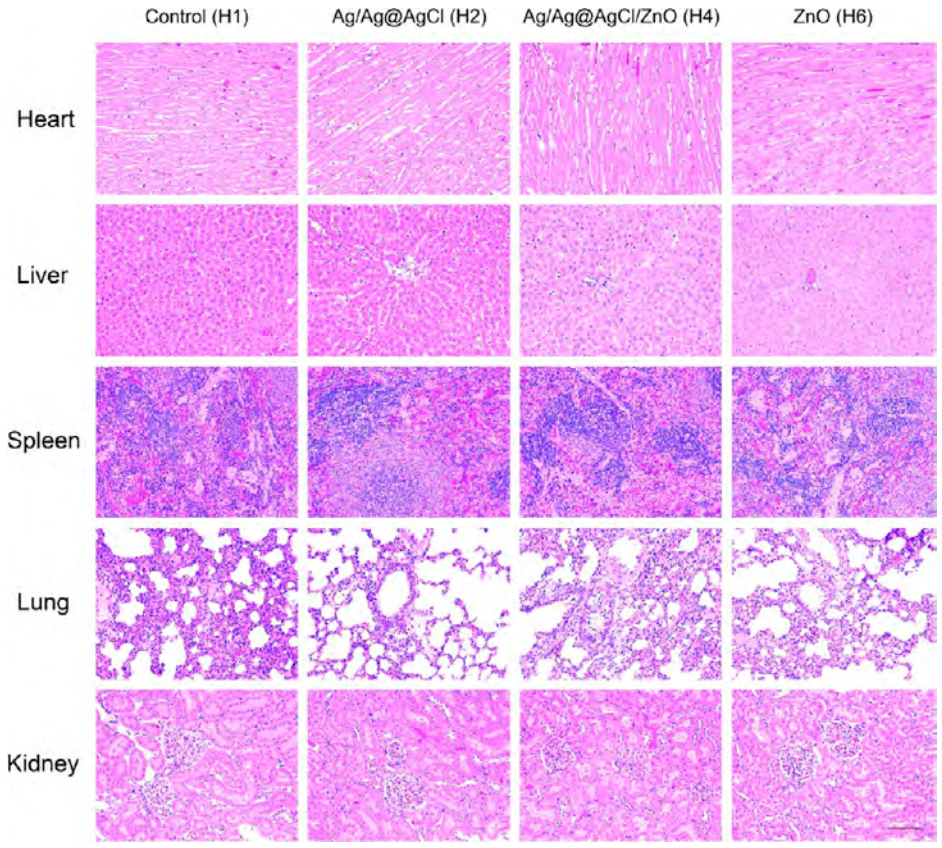

Figure 6. H&E staining of the heart, liver, spleen, lung, and kidney tissue slices after 14-day treatment for the different groups. Scale bar, 100 μm.

Hematoxylin and eosin (H&E) staining of the midportion of the repaired tissues is performed on days 2, 4, 8, and 14. Bacterial infection *in vivo* tends to stimulate the immune system to produce a large number of white blood cells (WBCs), especially neutrophils, for the antibacterial activity.[58−60] As shown in Figure 5B, many neutrophils (red arrows) appear from all the groups after the 2-day treatment, indicating a serious infection by *S. aureus*. Meanwhile, a large amount of dead cell debris (black arrows) and loose connective tissues with disorder in the collagen fibers (red rectangles) are observed from the control, Ag/Ag@AgCl groups, and groups with ZnO (Figure 5B). After the 4-day treatment, obvious dermal fibroblasts (green arrows) and newborn blood vessels (blue arrows) filled with a large number of red blood cells (cyan arrows) are observed first from the Ag/Ag@AgCl/ZnO group stemming from Zn^{2+} released from ZnO involved in the function of fibroblasts and production of more fibroblasts.[35,36] It is important that fibroblasts proliferate and differentiate into myofibroblasts in the dermis and subcutaneous tissues surrounding the wound during skin regeneration.[37−39] After the 8-day treatment, dermal fibroblasts (green arrows) and newborn blood vessels (blue arrows) are observed. Many neutrophils (red arrows) appear from groups I and II, and a large amount of connective tissue (black rectangles) is observed from the Ag/Ag@AgCl/ZnO group after the 8-day treatment. After the 14-day treatment, the wounds with ZnO (H4 and H6), especially the group of Ag/Ag@AgCl/ZnO (H4), heal but infected necrotic foci (cyan rectangles) appear from groups I and II, suggesting that the wounds have not yet healed. These results suggest that the *in vitro* cytotoxicity of Ag/Ag@AgCl/ZnO may not be used in the safety evaluation of the materials since it does not directly translate into wound healing *in vivo*.

Considering the different released amounts of Ag^{+} and Zn^{2+} from the different Ag/Ag@AgCl/ZnO nanocomposite hydrogels, the therapeutic efficacy with regard to wound healing of the H3 and H5 groups is studied, and the standard 3M wound dressing (conventional wound therapy, Minnesota Mining and Manufacturing Medical Equipment (Shanghai) Co., Ltd.) is implemented for comparison. As shown in Figure S20, the H3 group shows the best treatment effect than that of H4, but the 3M wound dressing is slightly worse because there is still a small amount of macrophages (green arrow in Figure S20) in H3. Edema and loose structures (red arrow in Figure S20) are observed from H5, and there is still focal coagulation necrosis (black arrow in Figure S20) in the case of the 3M wound dressing. The results suggest that the hydrogel embedded with the Ag/Ag@AgCl/ZnO nanostructures enhances skin regeneration. H4 shows the best therapeutic efficacy compared to the two groups of H3 and H5 with a similar structure as H4 on account of the better biocompatibility of H4 (Figure S18).

Not only the number of WBCs but also the number of neutrophils in the whole blood of the rats collected from all the treatment groups show obviously higher levels than the control group after the 4-day treatment. The same is true after the 8- and 14-day treatment, as shown in Figure 5C,D. It is believed that Ag^{+} and Zn^{2+} promote the immune functions and produce a large number of WBCs and neutrophils leading to the synergistic antibacterial activity. Furthermore, the histological analysis of the major organs (heart, liver, spleen, lung, and kidney) of mice does not indicate any abnormal effects or damage after the treatment (on day 14) as shown in Figures 6

DOI: 10.1021/acsnano.7b03513
ACS Nano 2017, 11, 9010−9021

and S22, indicating that the hydrogel constitutes a safe therapeutic system for wound healing.

CONCLUSION

An effective photodynamic therapy based on visible light irradiation of a hydrogel embedded with Ag/Ag@AgCl/ZnO hybrid nanostructures accelerates wound healing and mitigates bacterial infection. By taking advantage of the photogeneration of ROS, the system shows significantly enhanced photocatalytic activity, broad antibacterial activity against *E. coli* (Gram-negative) and *S. aureus* (Gram-positive), as well as accelerated wound healing. The hydrogel system which shows controllable and sustained release of Ag^+ and Zn^{2+} originating from the reversible swelling−shrinking transition triggered by changing pH has great potential in tissue repair and antibacterial applications.

EXPERIMENTAL SECTION

Silver and Zinc Ion Release. The amounts of Ag^+ and Zn^{2+} released from the nanocomposite hydrogels were determined in the phosphate-buffered saline (PBS) with pH of 7.4 and 5.6. The dried samples (ϕ5 mm × 2 mm) were immersed in 50 mL of PBS at 37 °C. At certain time intervals (1, 3, 7, 14, and 21 days), 1 mL of the solution was replaced with fresh PBS and withdrawn, and the amounts of released Ag^+ and Zn^{2+} were determined by inductively coupled plasma atomic emission spectrometry (ICP-AES, Optima 8000). The loading capacities of Ag and Zn were investigated by dissolving the samples in boiling concentrated nitric acid. The dried samples (ϕ5 mm × 2 mm) were immersed in 5 mL of concentrated nitric acid and heated to 300 °C. After the concentrated nitric acid was evaporated, 50 mL of deionized water was injected into the solution, and 3 mL of the solution was withdrawn to determine the concentrations of Ag^+ and Zn^{2+} by ICP-AES.

Electron Spin Resonance Spectroscopy. ROS, especially the hydroxyl radical (•OH) and singlet oxygen (O_2^1), are known to cause cellular damage including damage to cell membranes, cellular proteins, and even DNA.[56] The ROS measurements were carried out by electron spin resonance (ESR, JES-FA200) at room temperature. 2,2,6,6-Tetramethylpiperidine (TEMP) was used as a spin trap to detect singlet oxygen (O_2^1) during exposure of hydrogels to simulated sunlight, and 5,5-dimethyl-1-pyrroline-*N*-oxide (DMPO, 0.1 mol/L) was used to trap hydroxyl radicals (•OH) during irradiation. The spin traps were ESR silent but formed stable radicals with an ESR signal after donating electrons. The micro frequency was 8.93 GHz and power was 3 mW.

The dried samples (ϕ5 mm × 2 mm) were immersed in 200 μL of spin traps and irradiated by a 300 W xenon lamp (PLS-SXE300, Beijing Changming Technology Co,. LT, China) for 5 min. For comparison, the control group without samples or with H1 was also analyzed. The right amount of irradiated solution was put in a quartz capillary tube and sealed, and the sealed capillary tube was inserted into the ESR cavity to acquire the spectra.

***In Vitro* Antibacterial Activity Assay.** The hydrogels were subjected to two bacteria strains of *E. coli* (Gram-negative, ATCC 25922) and *S. aureus* (Gram-positive, ATCC 29213) at a concentration of *ca.* 1.0×10^7 CFU/mL. The antibacterial activity of Ag^+ and Zn^{2+} was studied using the agar diffusion test and optical density (OD) at 600 nm (Supporting Information). Nine mL of the melt solid media was inoculated with 1 mL of the bacterial stock suspension of *E. coli* and *S. aureus*, respectively, and evenly poured onto Petri dishes to solidify rapidly. The swelled hydrogels were placed on the agar plates and incubated at 37 °C in darkness for 12 h for *E. coli* and 24 h for *S. aureus*. The inhibition zone for bacterial growth was examined visually to monitor the antibacterial effect of the released Ag^+ and Zn^{2+}. To measure the OD at 600 nm, 300 μL of the bacterial suspension was added to each well with the samples and incubated at 37 °C in darkness for 12 h for *E. coli* and 24 h for *S. aureus*, respectively, with the H1 samples being the control. The bactericidal ratio was determined by eq 6.

$$\text{antibacterial ratio} = \frac{\text{control group OD} - \text{experimental group OD}}{\text{control group OD}} \times 100\% \quad (6)$$

The antibacterial activity of the hydrogels was further studied by the spread plating method, SEM (JSM6510LV), and TEM (Tecnai G20). The dried gels (ϕ5 mm × 2 mm) were placed on 96-well plates with the H1 samples as the control. 300 μL of the bacterial stock suspension was added to each well with samples. The 96-well plates containing the bacteria and hydrogels were irradiated by a 300 W xenon lamp for 20 min and incubated at 37 °C without light for 1 h under constant shaking. The bacteria in each well were diluted 200 times with the Luria−Bertani (LB) broth, and 10 μL of each dilution was collected, spread onto LB agar plates, and incubated at 37 °C for 24 h to form viable colony units. The bacteria survival ratio was calculated by eq 7:

$$\text{survival ratio} = \frac{\text{CFU(cell + gel + rad)} \times 100\%}{\text{CFU}_0\text{(cell)}} \quad (7)$$

where CFU (cell + gel + rad) was the area of the colony forming units measured in the presence of the dried gels and CFU_0 (cell) was the area of colony forming units measured in the presence of H1 but without simulated sunlight.

For SEM and TEM observation, the samples were processed by the same way as the 96-well plate test. The only difference was the incubation time of 8 h for samples for SEM observation and 24 h for TEM observation. After bacterial adhesion, the hydrogels were washed three times with PBS to remove nonadherent bacteria. The adherent bacteria on the hydrogels were fixed with 2.5% glutaraldehyde (25% glutaraldehyde:distilled water:PBS = 1:4:5) for 2 h, dehydrated by alcohol with different concentrations of 30, 50, 70, 90, and 100% orderly for 15 min, and freeze-dried overnight prior to SEM (JSM6510LV) observation. The bacterial suspensions after co-culturing with hydrogels for 24 h were withdrawn and centrifuged at 6000 rpm for 5 min. The condensed cells were fixed with 2.5% glutaraldehyde for 2 h and postfixed with 1% aqueous OsO_4 at room temperature for 2 h. Afterward, the samples were washed three times with PBS and dehydrated separately in an ascending ethanol series (30, 50, 70, 80, 90, and 100%) for 15 min before they were processed in the embedding medium (acetone: Epon 812 (SPI 90529-77-4) = 1:1) and pure Epon 812 orderly for 12 h. The samples were then embedded at 60 °C for 48 h. The sections (60−80 nm thick) were prepared with a microtome (Leica UC7) equipped with a diamond knife (Tecnai G2 20 TWIN) and stained with uranylacetate. Finally, the thin sections containing the cells were placed on copper grids for TEM (Tecnai G20) observation.

Cell Culture and MTT Assay. The experimental procedures for cell culture of mouse calvarial cells (MC3T3-E1) are described briefly in the following. The cells were cultured in the α-MEM (HyClone) medium containing 10% fetal bovine serum (FBS) and 1% penicillin-streptomycin solution (HyClone) at 37 °C in an incubator at 5% CO_2 and 95% humidity. The complete medium was replaced every 3 days, and confluent flasks were subcultured using trypsin.

In the MTT assay, the cells were seeded on the dried gels on 96-well plates with 300 μL of the medium. The medium was refreshed every 3 days with the H1 group as the control. After 1, 3, and 7 days, the culture medium was removed from each well, and 300 μL of the MTT solution (5 mg/mL in PBS) was added to each well and cultured at 37 °C for 4 h. Afterward, the MTT solution was replaced with 300 μL of dimethyl sulfoxide (DMSO), followed by shaking for 15 min. 200 μL of the supernatant from each well was transferred to a 96-well plate, and the absorbance was measured at 490 or 570 nm on a microplate reader (SpectraMax i3, Molecular Devices).

***In Vivo* Animal Experiments.** The *in vivo* animal experiments were approved by Wuhan Servicebio Technology Co., Ltd. China, and the male Wistar rats (180−200 g body weight) were obtained from Wuhan Centers for Disease Prevention & Control. The rats were

DOI: 10.1021/acsnano.7b03513
ACS Nano 2017, 11, 9010−9021

individually raised in cages at a standardized temperature for 2 days and evenly divided into four groups (each group containing five rats): control group (H1, group I), Ag/Ag@AgCl group (H2, group II), Ag/Ag@AgCl/ZnO group (H4 for representative, group III), and pure ZnO group (H6, group IV). The rats were anaesthetized by 10% chloral hydrate (30 mg/kg), and two partial thickness wounds were made on the right and left sides of the backbone with a surgical scalpel covering a rectangular surface (length of about 7 mm). The dried samples of four groups were soaked with 300 μL of *S. aureus* (1.0×10^7 CFU/mL) for 1 h, and the wounds of the four groups were tightly covered with soaked hydrogels (H1, H2, H4, and H6) using nonopaque sterile medical tapes. The rats were individually raised in cages at a standardized temperature on a 12:12 L/D cycle (lights on at 8 a.m.), and the wounds with hydrogels were irradiated by a 300 W xenon lamp for 10 min at 8 a.m. every 2 days. The hydrogels were changed every 2 days, and the process continued for 14 days with the soak solution being 0.9% NaCl instead of the *S. aureus* suspension. After 2, 4, 8, and 14 days, the wound areas were observed and photographed. The skin tissue samples were excised and fixed with 10% formalin to prepare the pathological slides. After staining with H&E, the histological images were acquired on an optical microscope (NIKON Eclipse Ci). Meanwhile, 20 μL of the exudate from the wound was collected on day 2, 4, and 8 and then diluted 100 times with the LB broth. Twenty μL of each dilution was collected and spread on the LB agar plate and incubated at 37 °C for 24 h to form viable colony units. Finally, 1 mL of whole blood was collected from the rat for routine analysis on a veterinary automatic blood cell analyzer (Mindray BC-2800 Vet). The major organs including the heart, liver, spleen, lung, and kidney were harvested and stained with H&E after the 14-day treatment.

Statistical Analysis. All data were evaluated as mean ± standard deviation based on at least three tests and contrasted via Kruskal–Wallis one-way analysis of variance (ANOVA).

ASSOCIATED CONTENT

Supporting Information

The Supporting Information is available free of charge on the ACS Publications website at DOI: 10.1021/acsnano.7b03513.

Experimental section (preparation and characterization of hydrogels; swelling behavior); results and discussion (swelling behavior; the effects of light intensity and wavelength on antibacterial activity; SEM images of hydrogel after wound therapy); supplementary table (fabrication processes of hydrogels) and figures (SEM images; TEM images; Zn^{2+}-response swelling profiles; diameter variation profile; cumulative Ag^+ release profiles; profiles of antibacterial effects of the ions; SEM images of bacteria; panels of formed viable colony units of bacteria; profiles of the effects of light intensity and wavelength on antibacterial activity; MTT profile; profiles of therapeutic effect of H3, H5, and 3M wound dressing); and references (PDF)

AUTHOR INFORMATION

Corresponding Author

*E-mail: shuilin.wu@gmail.com and shuilinwu@tju.edu.cn.

ORCID

Shuilin Wu: 0000-0002-1270-1870

Notes

The authors declare no competing financial interest.

ACKNOWLEDGMENTS

This work is jointly supported by the National Natural Science Foundation of China, nos. 51422102 and 81271715, National Key Research and Development Program of China no. 2016YFC1100600 (subproject 2016YFC1100604), Shenzhen Peacock Program (1108110035863317), Hong Kong Research Grants Council (RGC) General Research Funds (GRF) no. CityU 11301215, and City University of Hong Kong Applied Research Grant (ARG) no. 9667144.

REFERENCES

(1) Brogden, K. A. Antimicrobial Peptides: Pore Formers or Metabolic Inhibitors in Bacteria? *Nat. Rev. Microbiol.* **2005**, *3*, 238–250.

(2) Li, P.; Poon, Y. F.; Li, W.; Zhu, H. Y.; Yeap, S. H.; Cao, Y.; Qi, X.; Zhou, C.; Lamrani, M.; Beuerman, R. W.; Kang, E. T.; Mu, Y.; Li, C. M.; Chang, M. W.; Leong, S. S.; Chan-Park, M. B. A Polycationic Antimicrobial and Biocompatible Hydrogel with Microbe Membrane Suctioning Ability. *Nat. Mater.* **2011**, *10*, 149–156.

(3) Zhang, L. j.; Guerrero-Juarez, C. F.; Hata, T.; Bapat, S. P.; Ramos, R.; Plikus, M. V.; Gallo, R. L. Dermal Adipocytes Protect Against Invasive *Staphylococcus aureus* Skin Infection. *Science* **2015**, *347*, 67–71.

(4) Scherer, S.; Wagner, C.; Leuner, C.; Fleischer, W. Hydrogel. US patent US9415133, August 16, 2016.

(5) Liu, M.; Ishida, Y.; Ebina, Y.; Sasaki, T.; Aida, T. Photolatently Modulable Hydrogels Using Unilamellar Titania Nanosheets as Photocatalytic Crosslinkers. *Nat. Commun.* **2013**, *4*, 2029.

(6) Zhang, Y.; Liu, J.; Huang, L.; Wang, Z.; Wang, L. Design and Performance of a Sericin-Alginate Interpenetrating Network Hydrogel for Cell and Drug Delivery. *Sci. Rep.* **2015**, *5*, 12374.

(7) Perale, G.; Rossi, F.; Sundstrom, E.; Bacchiega, S.; Masi, M.; Forloni, G.; Veglianese, P. Hydrogels in Spinal Cord Injury Repair Strategies. *ACS Chem. Neurosci.* **2011**, *2*, 336–345.

(8) Hoffman, A. S. Hydrogels for Biomedical Applications. *Adv. Drug Delivery Rev.* **2012**, *64*, 18–23.

(9) Li, Y.; Rodrigues, J.; Tomás, H. Injectable and Biodegradable Hydrogels: Gelation, Biodegradation and Biomedical Applications. *Chem. Soc. Rev.* **2012**, *41*, 2193–2221.

(10) Li, Y.; Maciel, D.; Rodrigues, J.; Shi, X.; Tomás, H. Biodegradable Polymer Nanogels for Drug/Nucleic Acid Delivery. *Chem. Rev.* **2015**, *115*, 8564–8608.

(11) Li, Y.; Xiao, Y.; Liu, C. The Horizon of Materiobiology: A Perspective on Material-Guided Cell Behaviors and Tissue Engineering. *Chem. Rev.* **2017**, *117*, 4376–4421.

(12) Giano, M. C.; Ibrahim, Z.; Medina, S. H.; Sarhane, K. A.; Christensen, J. M.; Yamada, Y.; Brandacher, G.; Schneider, J. P. Injectable Bioadhesive Hydrogels with Innate Antibacterial Properties. *Nat. Commun.* **2014**, *5*, 4095.

(13) Liu, Y.; Ma, W. S.; Liu, W. W.; Li, C.; Liu, Y. L.; Jiang, X. Y.; Tang, Z. Y. Silver(I)-Glutathione Biocoordination Polymer Hydrogel: Effective Antibacterial Activity and Improved Cytocompatibility. *J. Mater. Chem.* **2011**, *21*, 19214–19218.

(14) Zheng, K.; Setyawati, M. I.; Lim, T. P.; Leong, D. T.; Xie, J. Antimicrobial Cluster Bombs: Silver Nanoclusters Packed with Daptomycin. *ACS Nano* **2016**, *10*, 7934–7942.

(15) Cha, S. H.; Hong, J.; McGuffie, M.; Yeom, B.; VanEpps, J. S.; Kotov, N. A. Shape-Dependent Biomimetic Inhibition of Enzyme by Nanoparticles and Their Antibacterial Activity. *ACS Nano* **2015**, *9*, 9097–9105.

(16) Zeng, X.; McCarthy, D. T.; Deletic, A.; Zhang, X. Silver/Reduced Graphene Oxide Hydrogel as Novel Bactericidal Filter for Point-of-Use Water Disinfection. *Adv. Funct. Mater.* **2015**, *25*, 4344–4351.

(17) Modi, S. R.; Lee, H. H.; Spina, C. S.; Collins, J. J. Antibiotic Treatment Expands the Resistance Reservoir and Ecological Network of the Phage Metagenome. *Nature* **2013**, *499*, 219–222.

(18) Li, L. L.; Xu, J. H.; Qi, G. B.; Zhao, X. Z.; Yu, F. Q.; Wang, H. Core-Shell Supramolecular Gelatin Nanoparticles for Adaptive and "On-Demand" Antibiotic Delivery. *ACS Nano* **2014**, *8*, 4975–4983.

(19) Davies, J. Inactivation of Antibiotics and the Dissemination of Resistance Genes. *Science* **1994**, *264*, 375–382.

DOI: 10.1021/acsnano.7b03513
ACS Nano 2017, 11, 9010–9021

(20) Kittler, S.; Greulich, C.; Diendorf, J.; Köller, M.; Epple, M. Toxicity of Silver Nanoparticles Increases During Storage Because of Slow Dissolution under Release of Silver Ions. *Chem. Mater.* **2010**, *22*, 4548−4554.
(21) Asharani, P. V.; Mun, G. L. K.; Hande, M. P.; Valiyaveettil, S. Cytotoxicity and Genotoxicity of Silver Nanoparticles in Human Cells. *ACS Nano* **2009**, *3*, 279−290.
(22) Zhu, P.; Weng, Z.; Li, X.; Liu, X.; Wu, S.; Yeung, K. W. K.; Wang, X.; Cui, Z.; Yang, X.; Chu, P. K. Biomedical Applications of Functionalized ZnO Nanomaterials: from Biosensors to Bioimaging. *Adv. Mater. Interfaces* **2016**, *3*, 1500494.
(23) Croucher, N. J.; Harris, S. R.; Fraser, C.; Quail, M. A.; Burton, J.; van der Linden, M.; McGee, L.; von Gottberg, A.; Song, J. H.; Ko, K. S.; Pichon, B.; Baker, S.; Parry, C. M.; Lambertsen, L. M.; Shahinas, D.; Pillai, D. R.; Mitchell, T. J.; Dougan, G.; Tomasz, A.; Klugman, K. P.; et al. Rapid Pneumococcal Evolution in Response to Clinical Interventions. *Science* **2011**, *331*, 430−434.
(24) Beaber, J. W.; Hochhut, B.; Waldor, M. K. SOS Response Promotes Horizontal Dissemination of Antibiotic Resistance Genes. *Nature* **2004**, *427*, 72.
(25) You, J.; Meng, L.; Song, T. B.; Guo, T. F.; Yang, Y. M.; Chang, W. H.; Hong, Z.; Chen, H.; Zhou, H.; Chen, Q.; Liu, Y.; De Marco, N.; Yang, Y. Improved Air Stability of Perovskite Solar Cells *via* Solution-Processed Metal Oxide Transport Layers. *Nat. Nanotechnol.* **2016**, *11*, 75−81.
(26) Choi, M. J.; Kim, S.; Lim, H.; Choi, J.; Sim, D. M.; Yim, S.; Ahn, B. T.; Kim, J. Y.; Jung, Y. S. Highly Asymmetric n^+-p Heterojunction Quantum-Dot Solar Cells with Significantly Improved Charge-Collection Efficiencies. *Adv. Mater.* **2016**, *28*, 1780−1787.
(27) Noimark, S.; Weiner, J.; Noor, N.; Allan, E.; Williams, C. K.; Shaffer, M. S. P.; Parkin, I. P. Dual-Mechanism Antimicrobial Polymer-ZnO Nanoparticle and Crystal Violet-Encapsulated Silicone. *Adv. Funct. Mater.* **2015**, *25*, 1367−1373.
(28) Li, Y.; Zhang, W.; Niu, J. F.; Chen, Y. S. Mechanism of Photogenerated Reactive Oxygen Species and Correlation with the Antibacterial Properties of Engineered Metal-Oxide Nanoparticles. *ACS Nano* **2012**, *6*, 5164−5173.
(29) He, W.; Kim, H. K.; Wamer, W. G.; Melka, D.; Callahan, J. H.; Yin, J. J. Photogenerated Charge Carriers and Reactive Oxygen Species in ZnO/Au Hybrid Nanostructures with Enhanced Photocatalytic and Antibacterial Activity. *J. Am. Chem. Soc.* **2014**, *136*, 750−757.
(30) Qin, B.; Chen, H. Y.; Liang, H.; Fu, L.; Liu, X. F.; Qiu, X. H.; Liu, S. Q.; Song, R.; Tang, Z. Y. Reversible Photoswitchable Fluorescence in Thin Films of Inorganic Nanoparticle and Polyoxometalate Assemblies. *J. Am. Chem. Soc.* **2010**, *132*, 2886−2888.
(31) Du, J.; Qi, J.; Wang, D.; Tang, Z. Y. Facile Synthesis of Au@ TiO2 Core−Shell Hollow Spheres for Dye-Sensitized Solar Cells with Remarkably Improved Efficiency. *Energy Environ. Sci.* **2012**, *5*, 6914−6918.
(32) Waiskopf, N.; Ben-Shahar, Y.; Galchenko, M.; Carmel, I.; Moshitzky, G.; Soreq, H.; Banin, U. Photocatalytic Reactive Oxygen Species Formation by Semiconductor-Metal Hybrid Nanoparticles. Toward Light-Induced Modulation of Biological Processes. *Nano Lett.* **2016**, *16*, 4266−4273.
(33) Samia, A. C. S.; Chen, X.; Burda, C. Semiconductor Quantum Dots for Photodynamic Therapy. *J. Am. Chem. Soc.* **2003**, *125*, 15736−15737.
(34) Ma, X. H.; Zhao, Y. Y.; Jiang, X. Y.; Liu, W.; Liu, S. Q.; Tang, Z. Y. Facile Preparation of Ag_2S/Ag Semiconductor/Metal Heteronanostructures with Remarkable Antibacterial Properties. *ChemPhysChem* **2012**, *13*, 2531−2535.
(35) Chen, C. C.; Keller, M.; Hess, M.; Schiffmann, R.; Urban, N.; Wolfgardt, A.; Schaefer, M.; Bracher, F.; Biel, M.; Wahl-Schott, C.; Grimm, C. A Small Molecule Restores Function to TRPML1 Mutant Isoforms Responsible for Mucolipidosis Type IV. *Nat. Commun.* **2014**, *5*, 4681.
(36) Ninan, N.; Forget, A.; Shastri, V. P.; Voelcker, N. H.; Blencowe, A. Anti-Bacterial and Anti-Inflammatory pH-Responsive Tannic Acid-Carboxylated Agarose Composite Hydrogels for Wound Healing. *ACS Appl. Mater. Interfaces* **2016**, *8*, 28511−28521.
(37) Bhang, S. H.; Jang, W. S.; Han, J.; Yoon, J. K.; La, W. G.; Lee, E.; Kim, Y. S.; Shin, J. Y.; Lee, T. J.; Baik, H. K.; Kim, B. S. Zinc Oxide Nanorod-Based Piezoelectric Dermal Patch for Wound Healing. *Adv. Funct. Mater.* **2017**, *27*, 1603497.
(38) Rouabhia, M.; Park, H.; Meng, S. Y.; Derbali, H.; Zhang, Z. Electrical Stimulation Promotes Wound Healing by Enhancing Dermal Fibroblast Activity and Promoting Myofibroblast Transdifferentiation. *PLoS One* **2013**, *8*, e71660.
(39) Sebastian, A.; Syed, F.; Perry, D.; Balamurugan, V.; Colthurst, J.; Chaudhry, I. H.; Bayat, A. Acceleration of Cutaneous Healing by Electrical Stimulation: Degenerate Electrical Waveform Down-Regulates Inflammation, Up-Regulates Angiogenesis and Advances Remodeling in Temporal Punch Biopsies in a Human Volunteer Study. *Wound Repair Regener.* **2011**, *19*, 693−708.
(40) Zhou, S.; Li, J.; Gilroy, K. D.; Tao, J.; Zhu, C.; Yang, X.; Sun, X.; Xia, Y. Facile Synthesis of Silver Nanocubes with Sharp Corners and Edges in an Aqueous Solution. *ACS Nano* **2016**, *10*, 9861−9870.
(41) Wu, Y. A.; Li, L.; Li, Z.; Kinaci, A.; Chan, M. K.; Sun, Y.; Guest, J. R.; McNulty, I.; Rajh, T.; Liu, Y. Visualizing Redox Dynamics of a Single Ag/AgCl Heterogeneous Nanocatalyst at Atomic Resolution. *ACS Nano* **2016**, *10*, 3738−3746.
(42) Shah, Z. H.; Wang, J.; Ge, Y.; Wang, C.; Mao, W.; Zhang, S.; Lu, R. Highly Enhanced Plasmonic Photocatalytic Activity of Ag/AgCl/TiO_2 by CuO Co-Catalyst. *J. Mater. Chem. A* **2015**, *3*, 3568−3575.
(43) Zhu, M. S.; Chen, P. L.; Liu, M. H. Graphene Oxide Enwrapped Ag/AgX (X = Br, Cl) Nanocomposite as a Highly Efficient Visible-Light Plasmonic Photocatalyst. *ACS Nano* **2011**, *5*, 4529−4536.
(44) An, C.; Peng, S.; Sun, Y. Facile Synthesis of Sunlight-Sriven AgCl: Ag Plasmonic Nanophotocatalyst. *Adv. Mater.* **2010**, *22*, 2570−2574.
(45) Marshall, J. L.; Telfer, S. J.; Young, M. A.; Lindholm, E. P.; Minns, R. A.; Takiff, L. A Silver-Free, Single-Sheet Imaging Medium Based on Acid Amplification. *Science* **2002**, *297*, 1516−1521.
(46) Patra, S.; Roy, E.; Karfa, P.; Kumar, S.; Madhuri, R.; Sharma, P. K. Dual-Responsive Polymer Coated Superparamagnetic Nanoparticle for Targeted Drug Delivery and Hyperthermia Treatment. *ACS Appl. Mater. Interfaces* **2015**, *7*, 9235−9246.
(47) Kozai, T. D.; Gugel, Z.; Li, X.; Gilgunn, P. J.; Khilwani, R.; Ozdoganlar, O. B.; Fedder, G. K.; Weber, D. J.; Cui, X. T. Chronic Tissue Response to Carboxymethyl Cellulose Based Dissolvable Insertion Needle for Ultra-Small Neural Probes. *Biomaterials* **2014**, *35*, 9255−9268.
(48) Yadollahi, M.; Namazi, H.; Barkhordari, S. Preparation and Properties of Carboxymethyl Cellulose/Layered Double Hydroxide Bionanocomposite Films. *Carbohydr. Polym.* **2014**, *108*, 83−90.
(49) Pacholski, C.; Kornowski, A.; Weller, H. Site-Specific Photodeposition of Silver on ZnO Nanorods. *Angew. Chem., Int. Ed.* **2004**, *43*, 4774−4777.
(50) Hsu, J. W. P.; Tian, Z. R.; Simmons, N. C.; Matzke, C. M.; Voigt, J. A.; Liu, J. Directed Spatial Organization of Zinc Oxide Nanorods. *Nano Lett.* **2005**, *5*, 83−86.
(51) Li, Y.; Liu, C. Nanomaterials-Based Bone Regeneration. *Nanoscale* **2017**, *9*, 4862−4874.
(52) Xiu, Z. M.; Zhang, Q. B.; Puppala, H. L.; Colvin, V. L.; Alvarez, P. J. Negligible Particle-Specific Antibacterial Activity of Silver Nanoparticles. *Nano Lett.* **2012**, *12*, 4271−4275.
(53) Wang, Y.; Song, S.; Liu, J.; Liu, D.; Zhang, H. ZnO-Functionalized Upconverting Nanotheranostic Agent: Multi-Modality Imaging-Guided Chemotherapy with On-Demand Drug Release Triggered by pH. *Angew. Chem.* **2015**, *127*, 546−550.
(54) Berk, V.; Fong, J. C. N.; Dempsey, G. T.; Develioglu, O. N.; Zhuang, X.; Liphardt, J.; Yildiz, F. H.; Chu, S. Molecular Architecture and Assembly Principles of Vibrio Cholerae Biofilms. *Science* **2012**, *337*, 236−239.
(55) Chen, Z.; Ji, H.; Liu, C.; Bing, W.; Wang, Z.; Qu, X. A Multinuclear Metal Complex Based DNase-Mimetic Artificial Enzyme:

DOI: 10.1021/acsnano.7b03513
ACS Nano 2017, 11, 9010−9021

Matrix Cleavage for Combating Bacterial Biofilms. *Angew. Chem., Int. Ed.* **2016**, *55*, 10732−10736.
(56) Applerot, G.; Lipovsky, A.; Dror, R.; Perkas, N.; Nitzan, Y.; Lubart, R.; Gedanken, A. Enhanced Antibacterial Activity of Nanocrystalline ZnO Due to Increased ROS-Mediated Cell Injury. *Adv. Funct. Mater.* **2009**, *19*, 842−852.
(57) Zhang, J.; Dong, G.; Thurber, A.; Hou, Y.; Gu, M.; Tenne, D. A.; Hanna, C. B.; Punnoose, A. Tuning the Properties of ZnO, Hematite, and Ag Nanoparticles by Adjusting the Surface Charge. *Adv. Mater.* **2012**, *24*, 1232−1237.
(58) Dopico, X. C.; Evangelou, M.; Ferreira, R. C.; Guo, H.; Pekalski, M. L.; Smyth, D. J.; Cooper, N.; Burren, O. S.; Fulford, A. J.; Hennig, B. J.; Prentice, A. M.; Ziegler, A. G.; Bonifacio, E.; Wallace, C.; Todd, J. A. Widespread Seasonal Gene Expression Reveals Annual Differences in Human Immunity and Physiology. *Nat. Commun.* **2015**, *6*, 7000.
(59) Tyrkalska, S. D.; Candel, S.; Angosto, D.; Gomez-Abellan, V.; Martin-Sanchez, F.; Garcia-Moreno, D.; Zapata-Perez, R.; Sanchez-Ferrer, A.; Sepulcre, M. P.; Pelegrin, P.; Mulero, V. Neutrophils Mediate Salmonella Typhimurium Clearance Through the GBP4 Inflammasome-Dependent Production of Prostaglandins. *Nat. Commun.* **2016**, *7*, 12077.
(60) Parodi, A.; Quattrocchi, N.; van de Ven, A. L.; Chiappini, C.; Evangelopoulos, M.; Martinez, J. O.; Brown, B. S.; Khaled, S. Z.; Yazdi, I. K.; Enzo, M. V.; Isenhart, L.; Ferrari, M.; Tasciotti, E. Synthetic Nanoparticles Functionalized with Biomimetic Leukocyte Membranes Possess Cell-Like Functions. *Nat. Nanotechnol.* **2013**, *8*, 61−68.

DOI: 10.1021/acsnano.7b03513
ACS Nano 2017, 11, 9010−9021

Supporting Information

Photo-Inspired Antibacterial Activity and Wound Healing Acceleration by Hydrogel Embedded with Ag/Ag@AgCl/ZnO Nanostructures

*Congyang Mao[a], Yiming Xiang[a], Xiangmei Liu[a], Zhenduo Cui[b], Xianjin Yang[b], Kelvin Wai Kwok Yeung[c], Haobo Pan[d], Xianbao Wang[a], Paul K Chu[e], Shuilin Wu[a,b]**

[a] Hubei Collaborative Innovation Center for Advanced Organic Chemical Materials, Ministry-of-Education Key Laboratory for the Green Preparation and Application of Functional Materials, Hubei Key Laboratory of Polymer Materials, School of Materials Science & Engineering, Hubei University, Wuhan 430062, China

[b] School of Materials Science & Engineering, Tianjin University, Tianjin 300072, China

[c] Department of Orthopaedics & Traumatology, Li Ka Shing Faculty of Medicine, The University of Hong Kong, Pokfulam, Hong Kong, China

[d] Center for Human Tissues and Organs Degeneration, Shenzhen Institutes of Advanced Technology, Chinese Academy of Sciences, Shenzhen 518055, China

[e] Department of Physics and Department of Materials Science and Engineering, City University of Hong Kong, Tat Chee Avenue, Kowloon, Hong Kong, China

* To whom correspondence should be addressed:

E-mail: shuilin.wu@gmail.com; shuilinwu@tju.edu.cn (S.L. Wu)

Table of contents

1. Experimental section

1.1 Preparation of the CMC hydrogel

To prepare the CMC hydrogels in a 250 mL three-neck round bottom flask, 3 g of CMC were dissolved in 100 mL of 3% W/V NaOH under continuous stirring for 30 min to obtain a homogenous viscous mixture. 6 mL of epichlorohydrin (ECH) were added drop-wise with a funnel and stirred for 2 h until a homogenous mixture was obtained. The mixture was poured onto a glass petri dish with a diameter of 15 cm and heated to 80 ^{o}C for 2 h to achieve better prepolymerization. The prepolymer was collected and washed several times with distilled water to remove residual NaOH and ECH and dried in an oven at 50 ^{o}C for 24 h until a white solid dried gel was obtained.

1.2 Fabrication of the Ag/Ag@AgCl/ZnO embedded hydrogels

The obtained dried gel was cut with a mold to obtain slices with a regular shape and uniform size of $\phi 18\,mm \times 1\,mm$ (0.12 g). The samples were immersed in 100 mL of distilled water for 12 h for water-absorption swelling to open the pores in the gel. The swollen gel samples were immersed in 100 mL of silver nitrate ($AgNO_3$) with different concentrations (0.00, 2.50 mM, 0.75 mM, 1.25 mM, and 2.50 mM) to incorporate Ag^+ and part of Ag^+ combined with Cl^- in the hydrogels to form silver chloride (AgCl). In order to load Zn^{2+}, the swollen hydrogel plate was put in 100 mL of zinc nitrate ($Zn(NO_3)_2$) with a concentration of 5 mM for 12 h. The hydrogel samples were divided into six groups, group 1, group 2, group 3, group 4, group 5, and group 6 with 3 samples in each group. The samples were rinsed with distilled water thoroughly to remove Ag^+ and Zn^{2+} attached to the surface. After cleaning, group 1 was freeze-dried overnight to obtain the dry gel. Group 6 was placed in 100 mL of 0.01 M NaOH for 4 h to obtain ZnO produced by combination of the hydroxide ion and loaded Zn^{2+} and this group was rinsed with distilled water to remove residual

NaOH and freeze-dried overnight to obtain the dry ZnO nanocomposite hydrogels. The other 4 groups (2, 3, 4, and 5) were illuminated with UV light (λ = 365 nm) for 2 h to obtain Ag NPs from reduction of the loaded Ag^+ and AgCl. Group 2 was freeze-dried overnight to obtain the dry Ag/Ag@AgCl nanocomposite hydrogels. Groups 3, 4, and 5 were placed in 100 mL of 5 mM of $Zn(NO_3)_2$ for 12 h and the subsequent processes were the same as that for group 6 followed by freeze-drying overnight to obtain the dry Ag/Ag@AgCl/ZnO nanocomposite hydrogels. The products were labeled as H1, H2, H3, H4, H5, and H6 as shown in Table S1.

1.3 Characterization of the nanocomposite hydrogels

To determine the phase structure, the dried gels with different concentrations of initial $AgNO_3$ were analyzed by X-ray diffraction (XRD, D8A25, Bruker, Germany) in the continuous mode with 2θ scanned from 20^o to 80^o, step size of 0.02^o, and incident angle of 3^o. The morphology and composition of the dried gels were determined by a scanning electron microscopy (SEM, JSM7100F and JSM6510LV) equipped with an energy-dispersive X-ray spectrometer (EDS). The microstructure of the dried gels was investigated by transmission electron microscope (TEM, Tecnai G20) and selected-area electron diffraction (SAED).

1.4 Swelling behavior

To facilitate the swelling tests and biological assay, the samples (H1, H2, H3, H4, H5, and H6) were cut into circular pieces with dimensions of $\phi 5mm \times 2mm$ (0.7 mg). The samples were immersed in 10 mL of aqueous solutions with a series of pH at room temperature for 24 h to reach the swelling equilibrium. The swelling ratio of the hydrogels was calculated by Eq. (1).

$$\text{Swelling ratio} = \frac{(W - W_0) * 100\%}{W_0} \quad (1),$$

where W_0 was the initial weight of the dried gels and W was the weight of the samples after swelling for 24 h. To prepare the different pH media, the HCl (1.0 M) and NaOH (1.0 M) solutions were diluted with distilled water to reach the pre-designated pH of 2, 3, 4, 5.6, 7, 8, 9, or 10.

2. Results and discussion

2.1 Swelling behavior

The swelling ratios of all hydrogels increase as the pH goes up from 2 to 8 but decreases when the pH is over 8. This is caused by the carboxylate groups on the polymer chains being protonated at a low pH to eliminate the anion-anion repulsive forces. Water molecules are taken out to decrease the swelling ratio. When the pH reaches 8, the carboxylate groups are ionized resulting in electrostatic repulsion between the carboxylate groups and the maximum swelling capacity. However, in the more basic solutions (pH = 9 and 10), the ionic strength of the medium increases and as a result, the carboxylate groups are shielded by the counter ions from the solution thus preventing electrostatic repulsion and decreasing the swelling ratio.

The swelling ratio of H6 is less than that of H2 at low pH (< 6) due to ZnO NPs in H6. When the ZnO NPs are dissolved in the acidic solutions, they produce a large number of zinc ions and part of Zn^{2+} with two positive charges is bound to two carboxylate groups on the adjacent two chains as shown in Figure S7a. This produces compressing force between the two chains to decrease the swelling ratio. The force is eliminated when the pH is over 7 because the ZnO NPs remaining in the solutions produce a larger swelling ratio for H6 than H2. As shown in Figure S7b, the CMC hydrogel swells after water absorption but shrinks in the presence of Zn^{2+}. The corresponding optical images in Figure S7c provide further evidence about this phenomenon. The diameter of the hydrogel increases from 5 mm to 17 mm after water absorption but

decreases to 13 mm in the presence of Zn^{2+}. The Zn^{2+} response makes it possible for the CMC hydrogel to be a special carrier in drug delivery systems. Furthermore, the corresponding optical images in Figure S8 illustrate the rapid reversible swelling-shrinking behavior of the hydrogels, indicating that they are promising in drug delivery systems, tissue engineering, sensing systems, smart coating materials, and so on.[1-3]

2.2 Effects of light intensity and wavelength on the antibacterial activity

H2 is selected to study the effects of light intensity and wavelength on the antibacterial activity due to its excellent photocatalytic property. As shown in Figure S16A, as the visible light intensity is increased, the number of colony units decreases and the antibacterial ratio of H2 increases gradually (Figure S16B). Moreover, H2 delivers excellent antibacterial performance after irradiation with a 200 W xenon lamp with wavelengths over 300 nm or over 410 nm (controlled by the optical filter) as shown in Figure S17. The antibacterial effect of H2 diminishes when the wavelength is larger than 510 nm, especially over 600 nm and over 800 nm, indicating that light with the wavelength range of 300-510 nm is crucial to the antimicrobial and photocatalytic activity of the Ag/Ag@AgCl hybrid nanostructures (H2).

2.3 SEM images of the hydrogel after wound therapy

The SEM images of the Ag/Ag@AgCl/ZnO nanocomposite hydrogels after wound healing in the animal models are depicted in Figure S21. The Ag@AgCl nanostructures (Figure S21A) are still intact while both Ag and ZnO are reduced sharply and even disappear due to the acidic environment arising from inflammation during the wound healing process. Both the Ag NPs and ZnO can dissolve in the acidic environment and it is consistent with the ion release behavior presented in

Figure 3.

3. Supplementary Table and Figures

	Step 1	Step 2	Step 3	Step 4	Step 5
H1	H_2O 12 h	—	—	—	—
H2	H_2O 12 h	$AgNO_3$ 2.5 mM 12 h	UV 2 h	—	—
H3	H_2O 12 h	$AgNO_3$ 0.75 mM 12 h	UV 2 h	$Zn(NO_3)_2 \cdot 6H_2O$ 5 mM 12 h	NaOH 0.01 M 4 h
H4	H_2O 12 h	$AgNO_3$ 1.25 mM 12 h	UV 2 h	$Zn(NO_3)_2 \cdot 6H_2O$ 5 mM 12 h	NaOH 0.01 M 4 h
H5	H_2O 12 h	$AgNO_3$ 2.5 mM 12 h	UV 2 h	$Zn(NO_3)_2 \cdot 6H_2O$ 5 mM 12 h	NaOH 0.01 M 4 h
H6	H_2O 12 h	$Zn(NO_3)_2 \cdot 6H_2O$ 5 mM 12 h	NaOH 0.01 M 4 h	—	—

Table S1. Fabrication process for the different nanocomposite hydrogels.

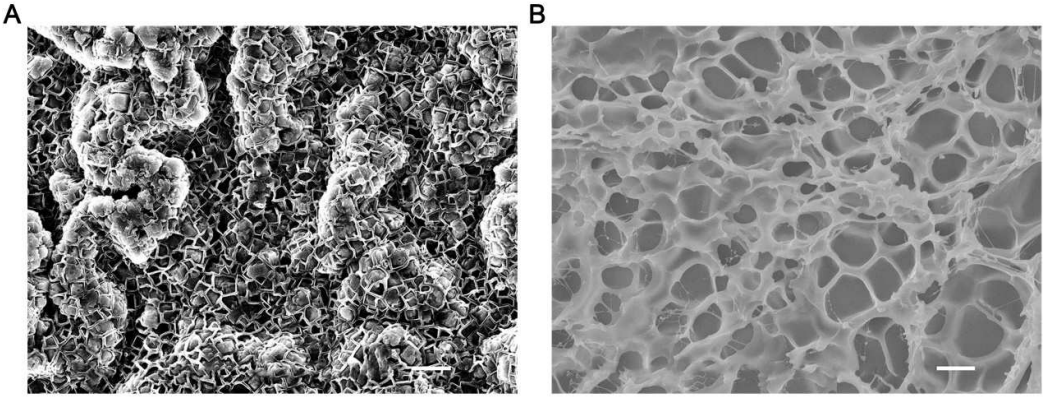

Figure S1. Typical SEM images of the networks in the CMC hydrogel of (A) not swollen and (B) Swollen after water absorption (Scale bars = 10 μm).

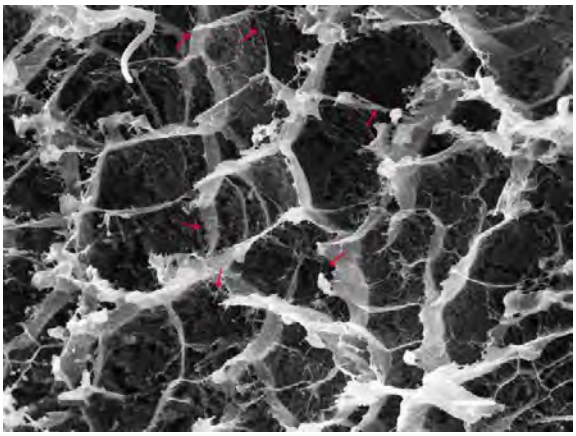

Figure S2. SEM images of the damaged networks in the CMC hydrogel (Scale bar = 10 μm).

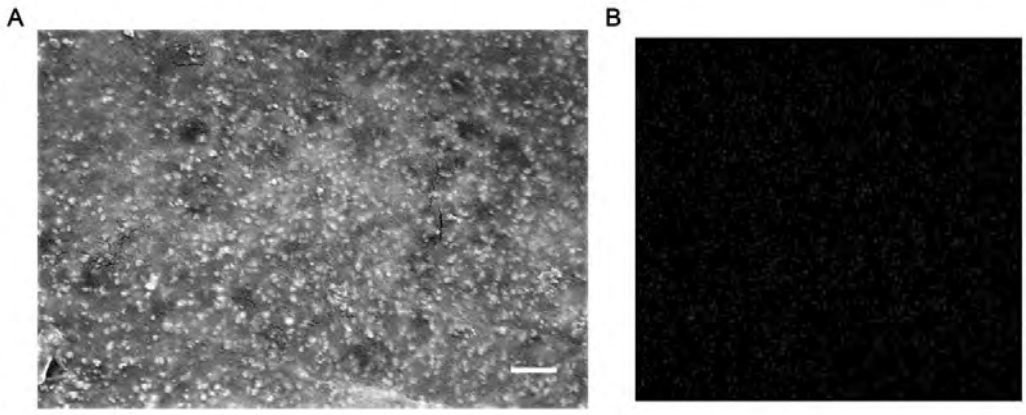

Figure S3. SEM images of (A) Ag nanoparticles in hydrogel and (B) Corresponding elemental area scan by EDS (Scale bar = 1 μm).

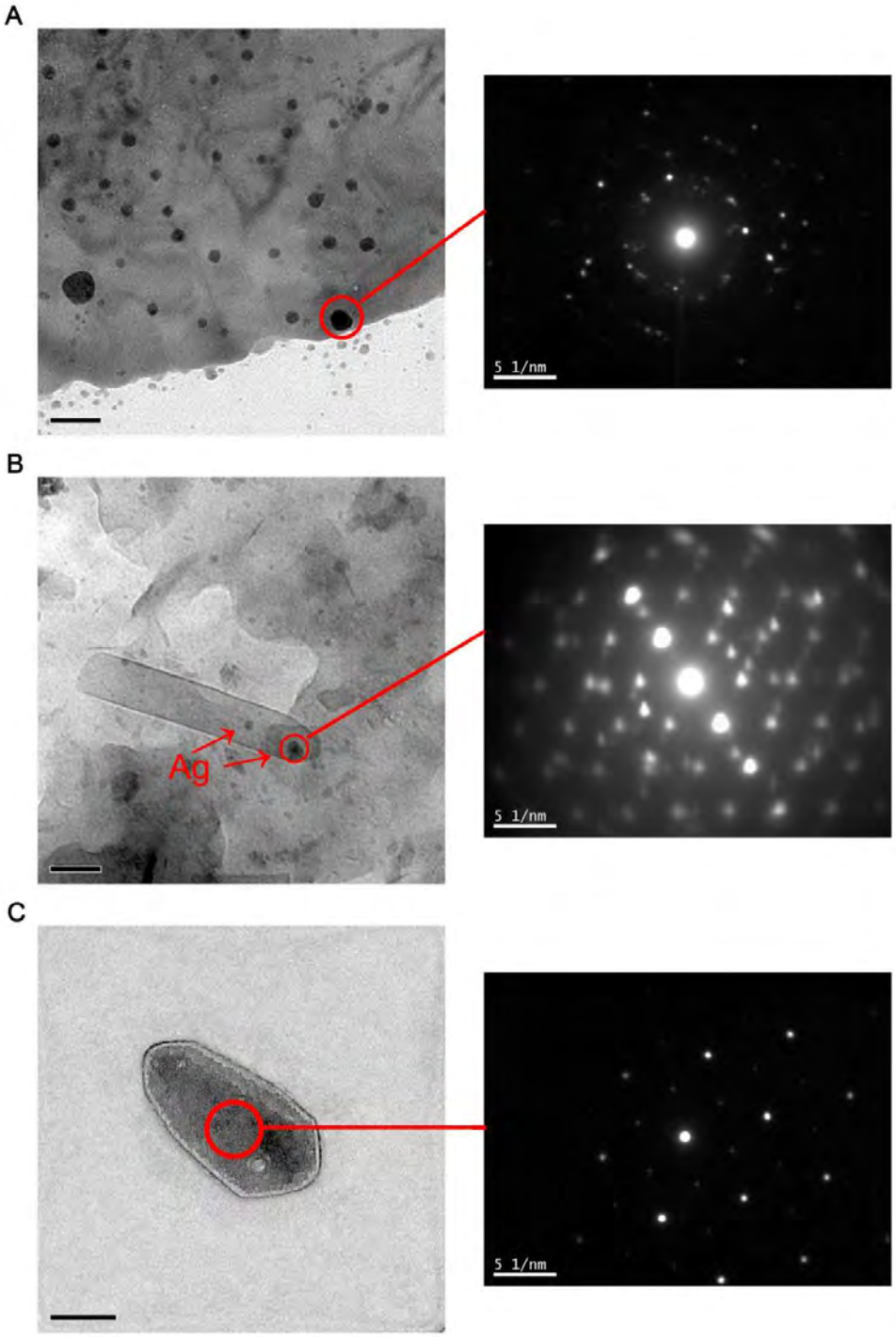

Figure S4. TEM image of (A) Ag nanoparticles, (B) Ag nanoparticles incorporated into the ZnO nanorods (Scale bars = 50 nm.), and (C) ZnO nanoparticles in the hydrogels. The insets are the corresponding SAED results (Scale bar = 100 nm).

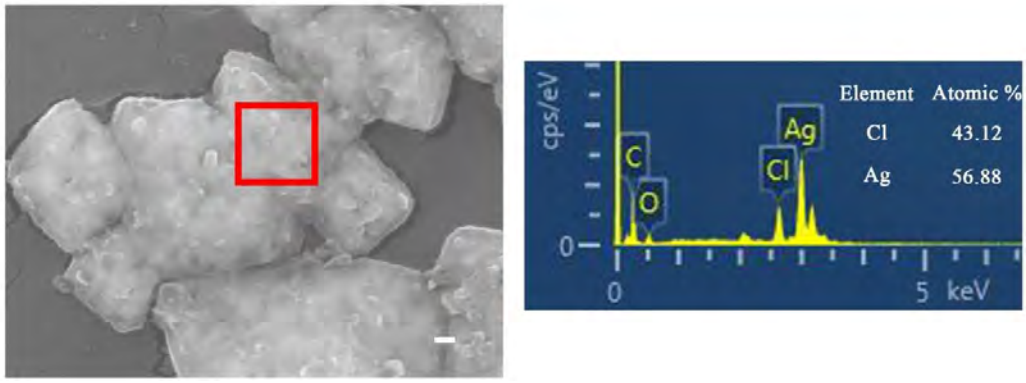

Figure S5. EDS analysis of Ag@AgCl nanostructures (Scale bar = 100 nm).

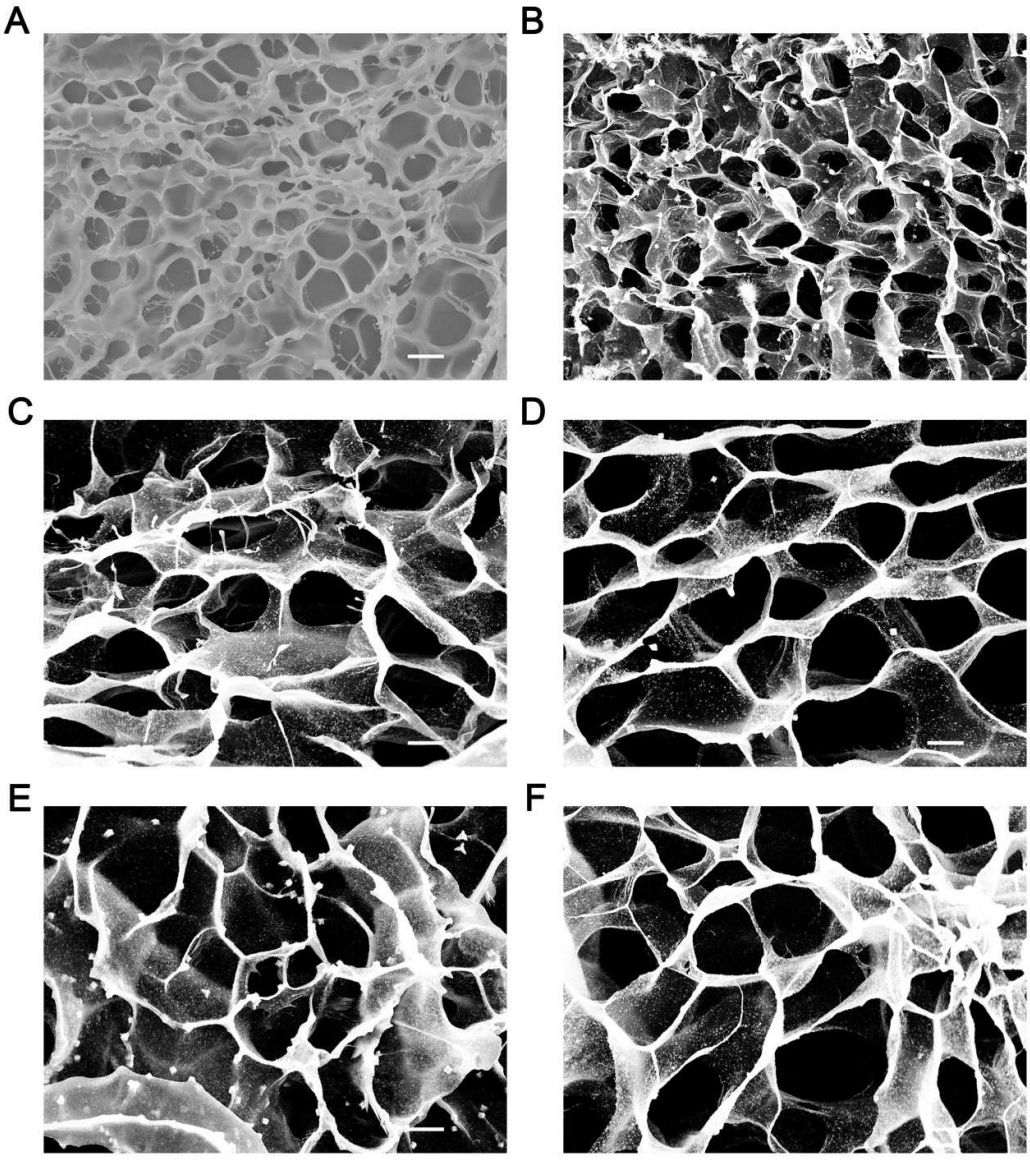

Figure S6. Typical SEM images of the networks in the hydrogels of (A) H1, (B) H2, (C) H3, (D) H4, (E) H5 and (F) H6 (Scale bars = 10 μm).

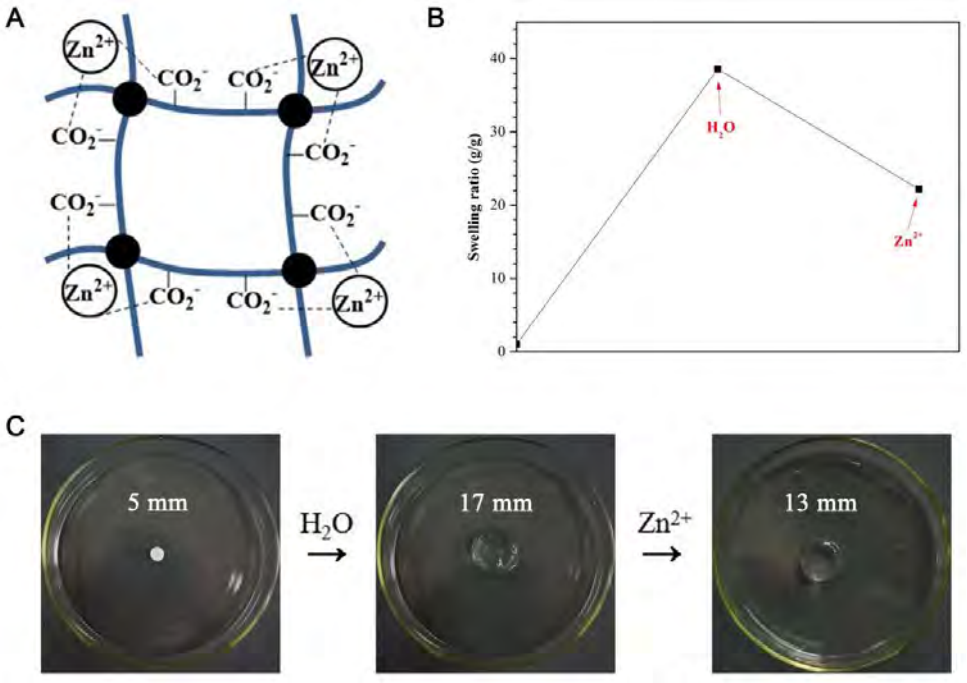

Figure S7. (A) Combination of Zn^{2+} with the networks of hydrogel, (B) Zn^{2+} responsive swelling, and (C) Corresponding optical images.

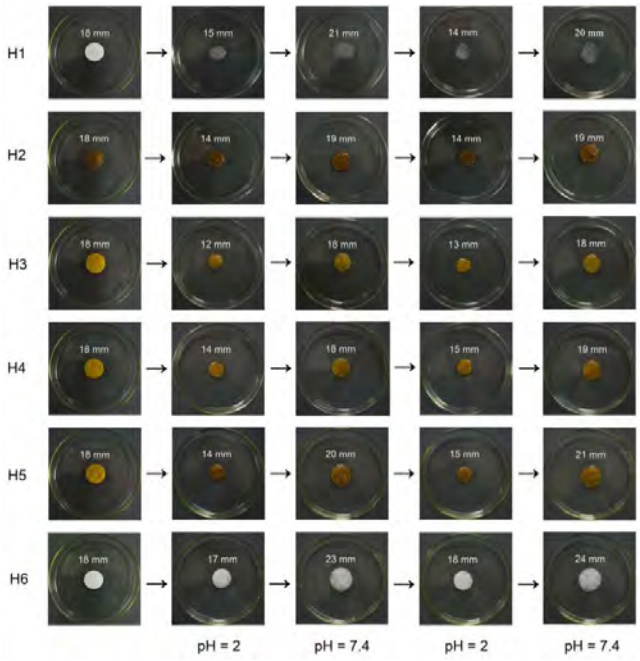

Figure S8. Optical images corresponding to the cyclic pH-stimulated transitions of hydrogels between pH changes from 2 to 7.4 with 1-min intervals.

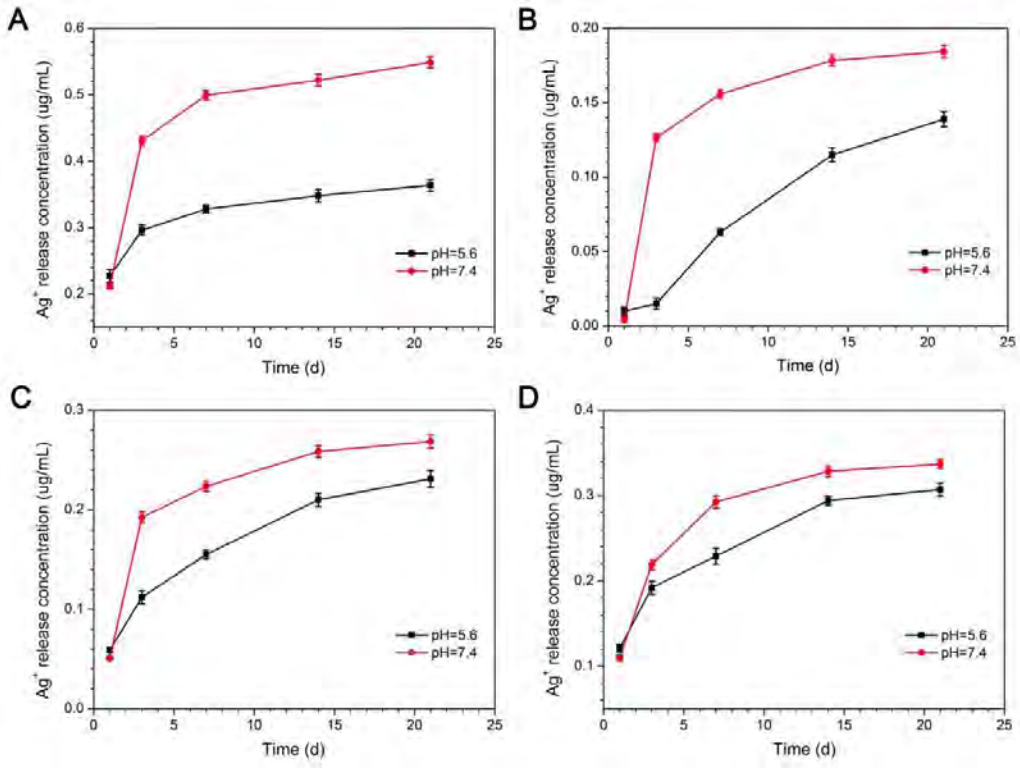

Figure S9. Cumulative silver ion release profiles acquired from the nanocomposite hydrogels: (A) H2, (B) H3, (C) H4 and (D) H5 in pH 7.4 and 5.6 PBS. The experiment was performed in triplicate and independently (n = 3) with data being mean ± SD.

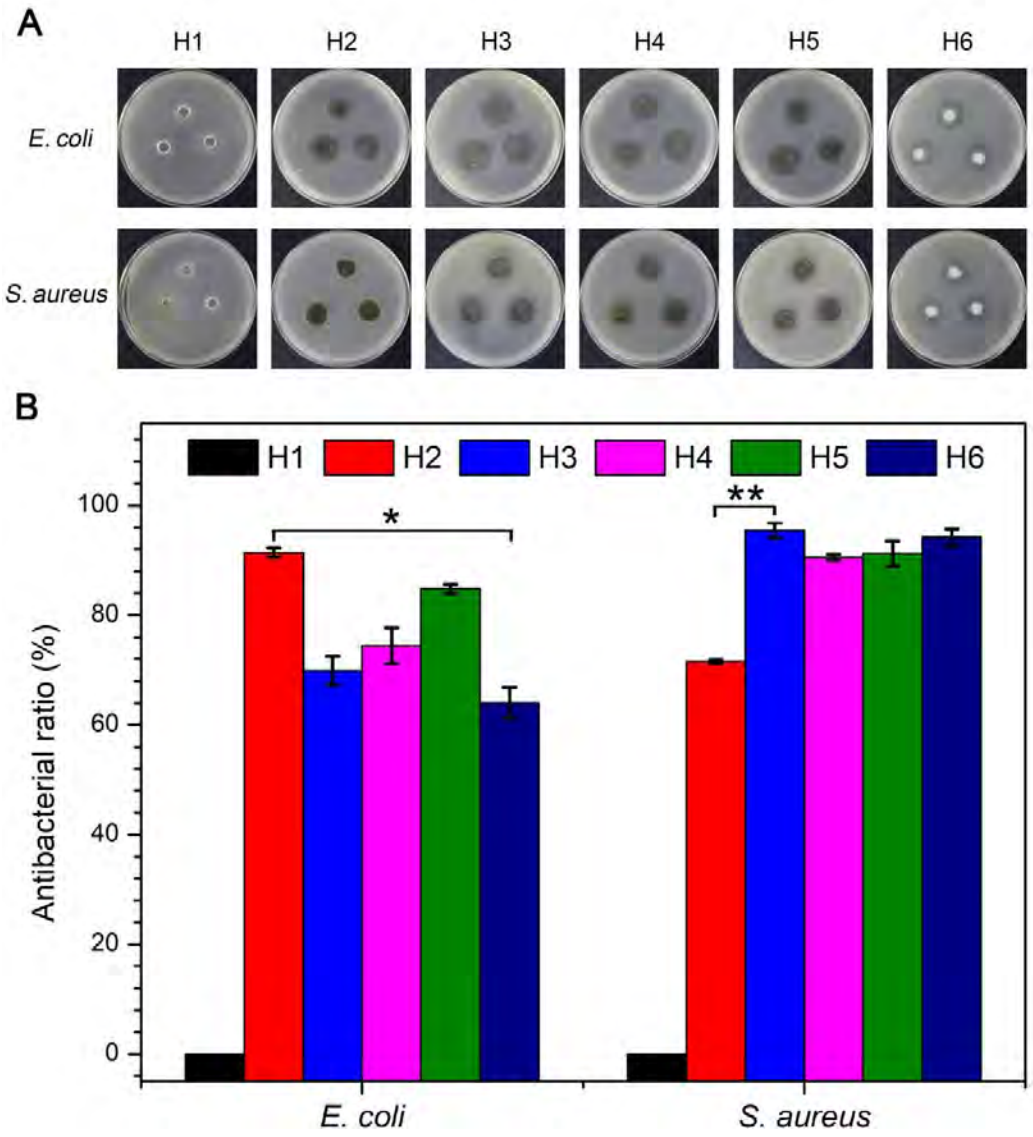

Figure S10. (A) Formed inhibition zones of swollen hydrogels of H1, H2, H3, H4, H5, and H6 against *E. coli* and *S. aureus* after incubation at 37°C in darkness for 12 h for *E. coli* and 24 h for *S. aureus*; (B) Antibacterial effects of the ions released from the different samples in darkness for 12 h for *E. coli* and 24 h for *S. aureus*. The experiment was performed in triplicate and independently (n = 3) with data being mean ± SD.

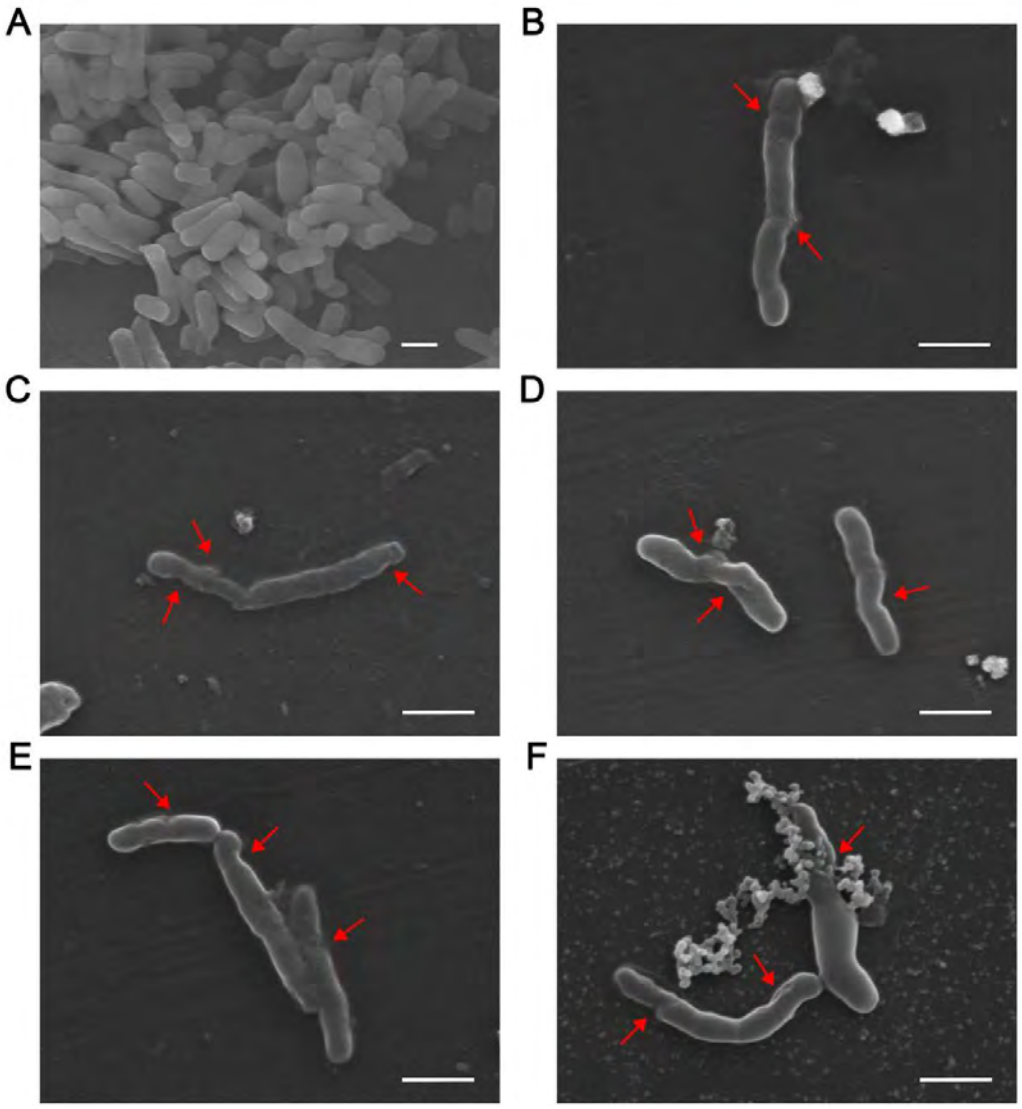

Figure S11. SEM images of *E. coli* treated with (A) H1, (B) H2, (C) H3, (D) H4, (E) H5 and (F) H6 (Scale bars = 1 μm).

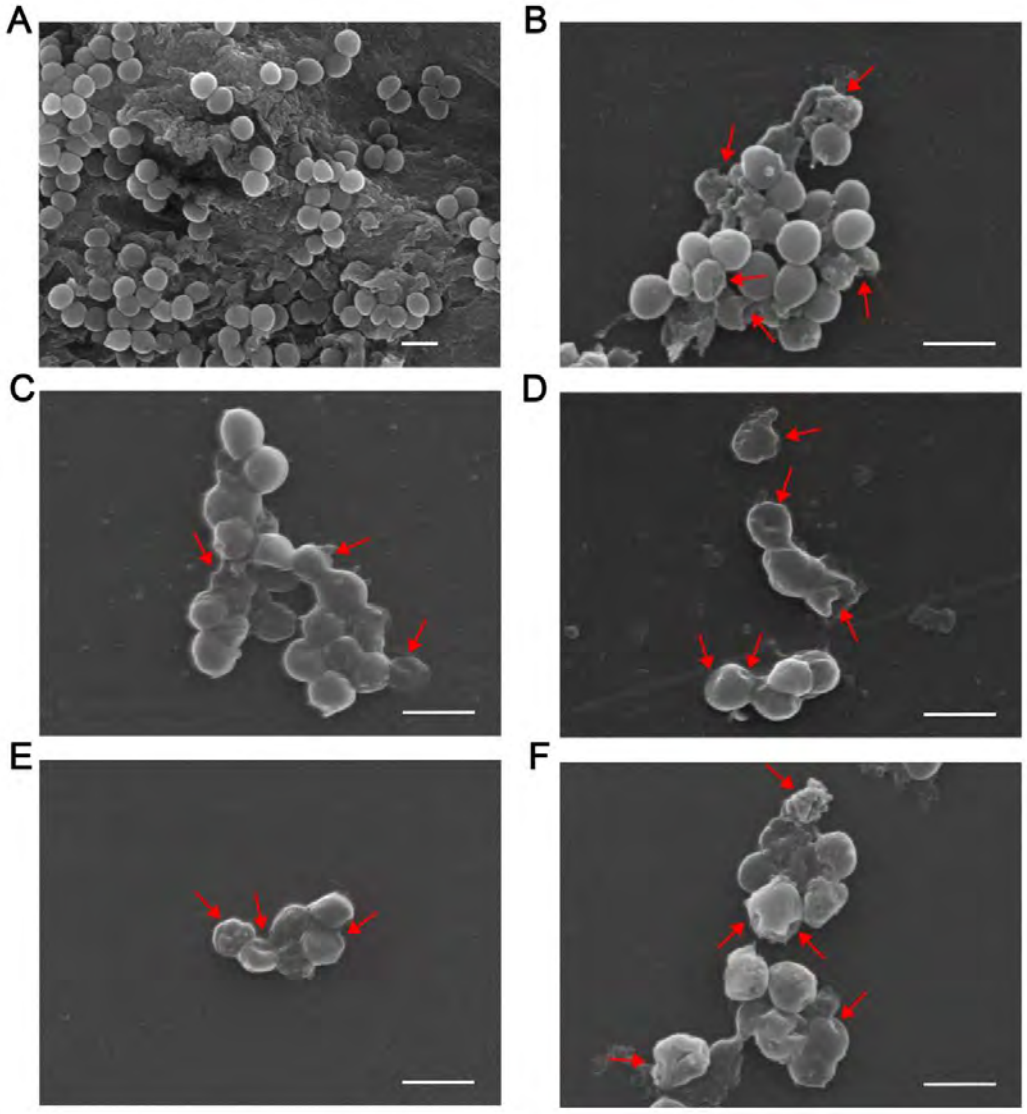

Figure S12. SEM images of *S. aureus* treated with (A) H1, (B) H2, (C) H3, (D) H4, (E) H5 and (F) H6 (Scale bars = 1 μm).

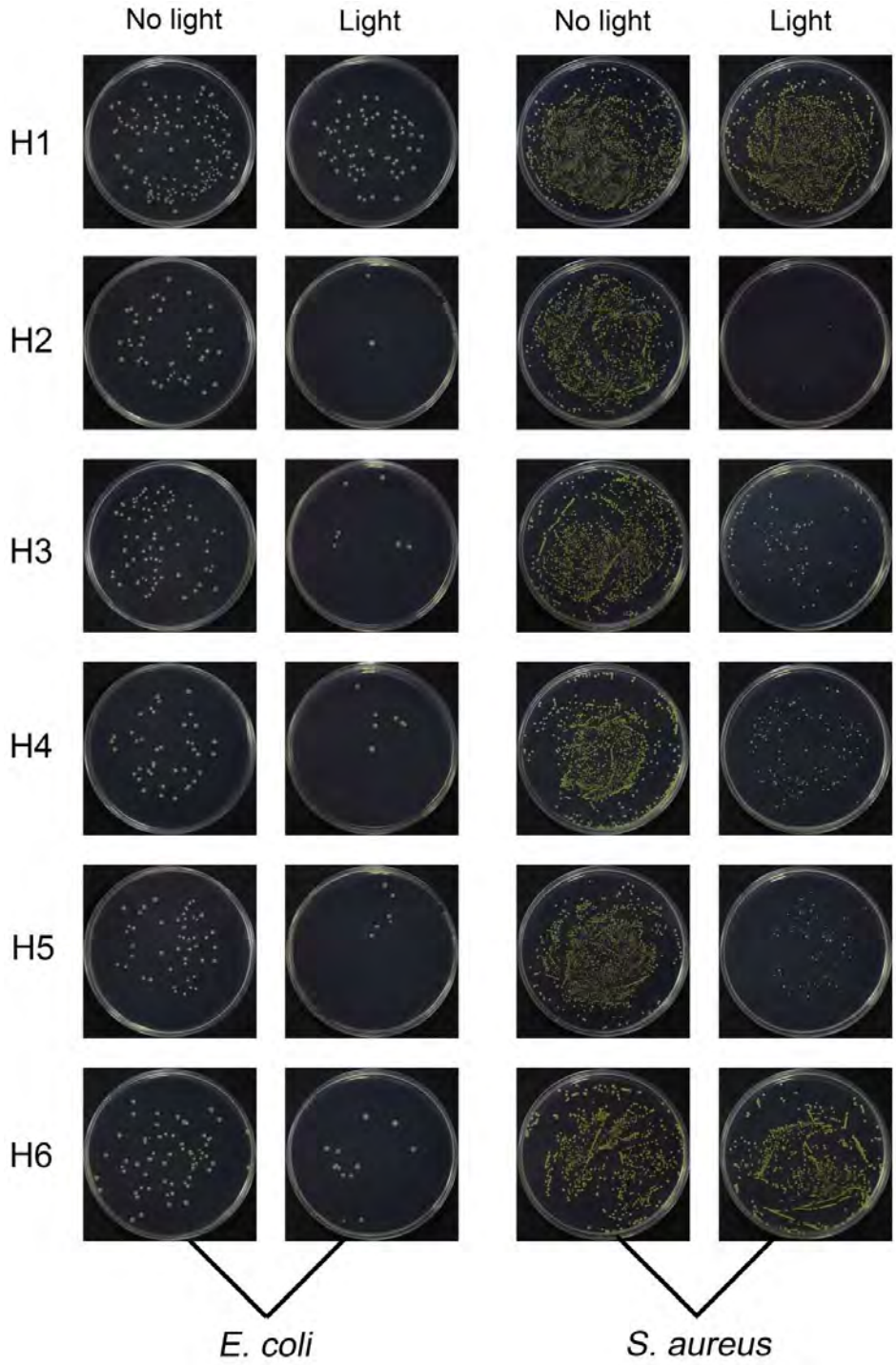

Figure S13. Formed viable colony units of *E. coli* (left) and *S. aureus* (right) after treatment with hydrogels under visible light or without light for 20 min, incubated at 37 °C in darkness for 1 hour, diluted 200 times, spread on LB agar plates, and incubated at 37 °C for 24 h.

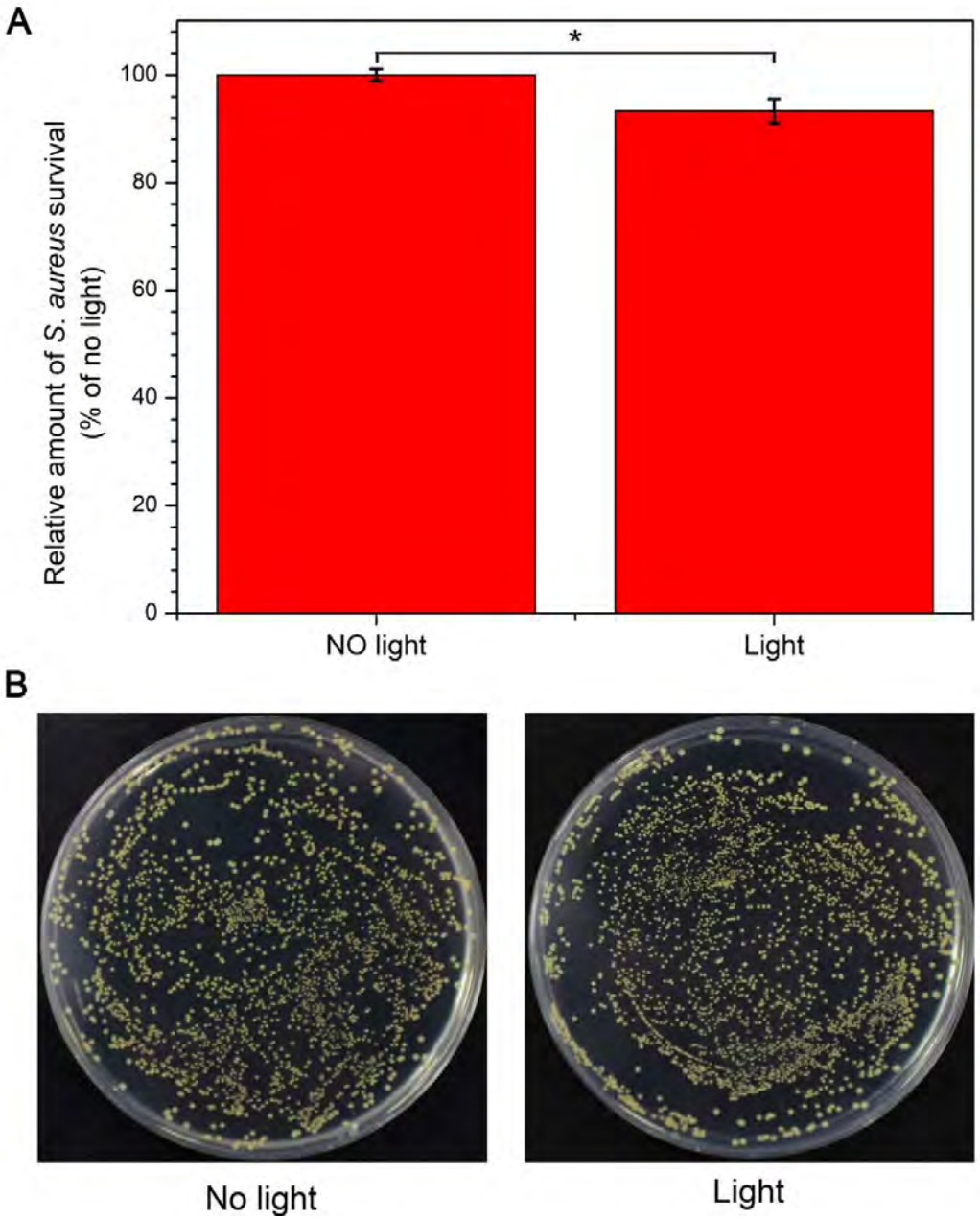

Figure S14. (A) Survival ratios of *S. aureus* before and after light illumination; **(B)** Corresponding formed viable colony units. The experiment was performed in triplicate and independently (n = 3) with data being mean ± SD.

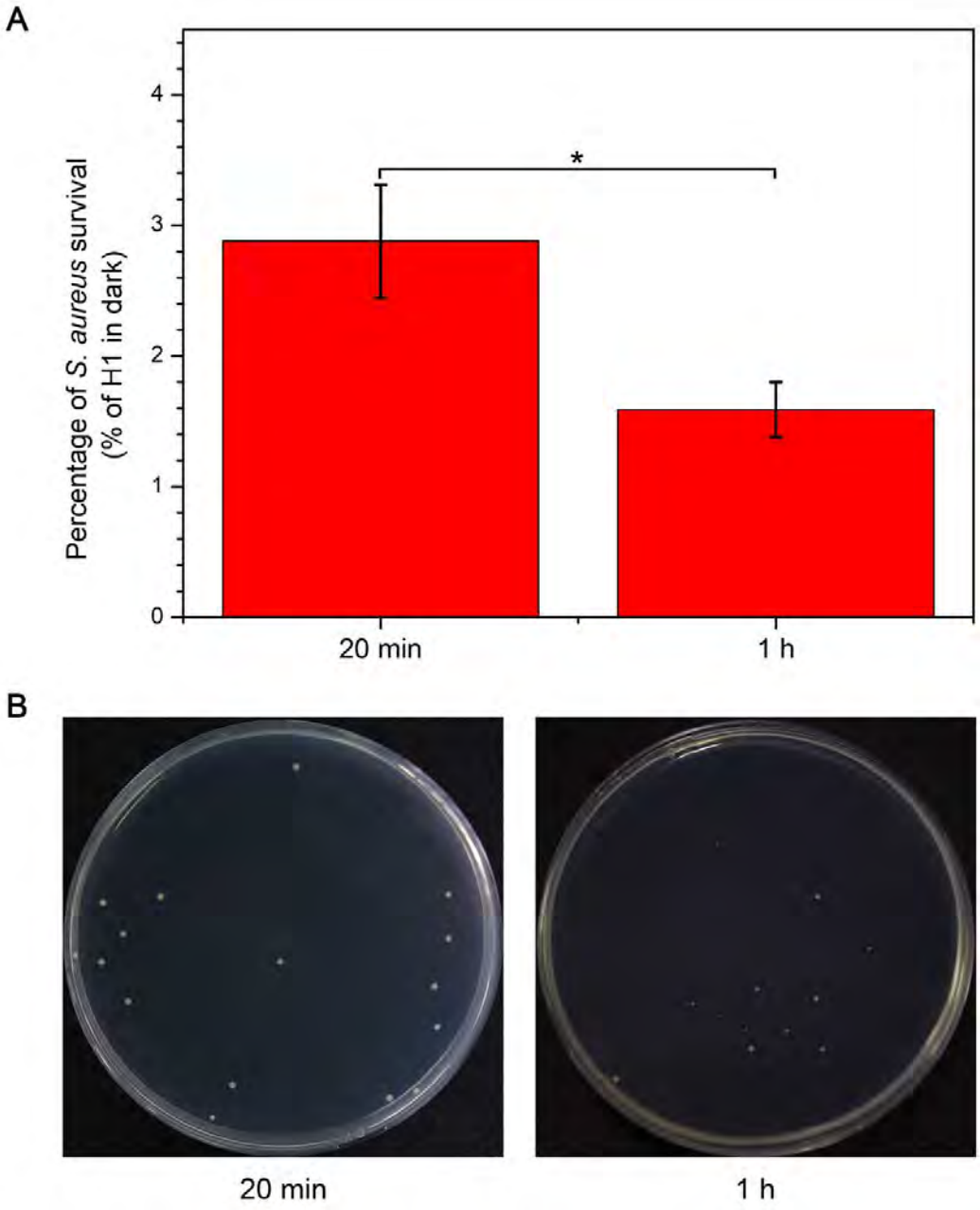

Figure S15. (A) Survival ratios of *S. aureus* after exposure to H2 and simulated sunlight for only 20 min and for 20 min (with 1 h in darkness); (B) Corresponding formed viable colony units. The experiment was performed in triplicate and independently (n = 3) with data being mean ± SD.

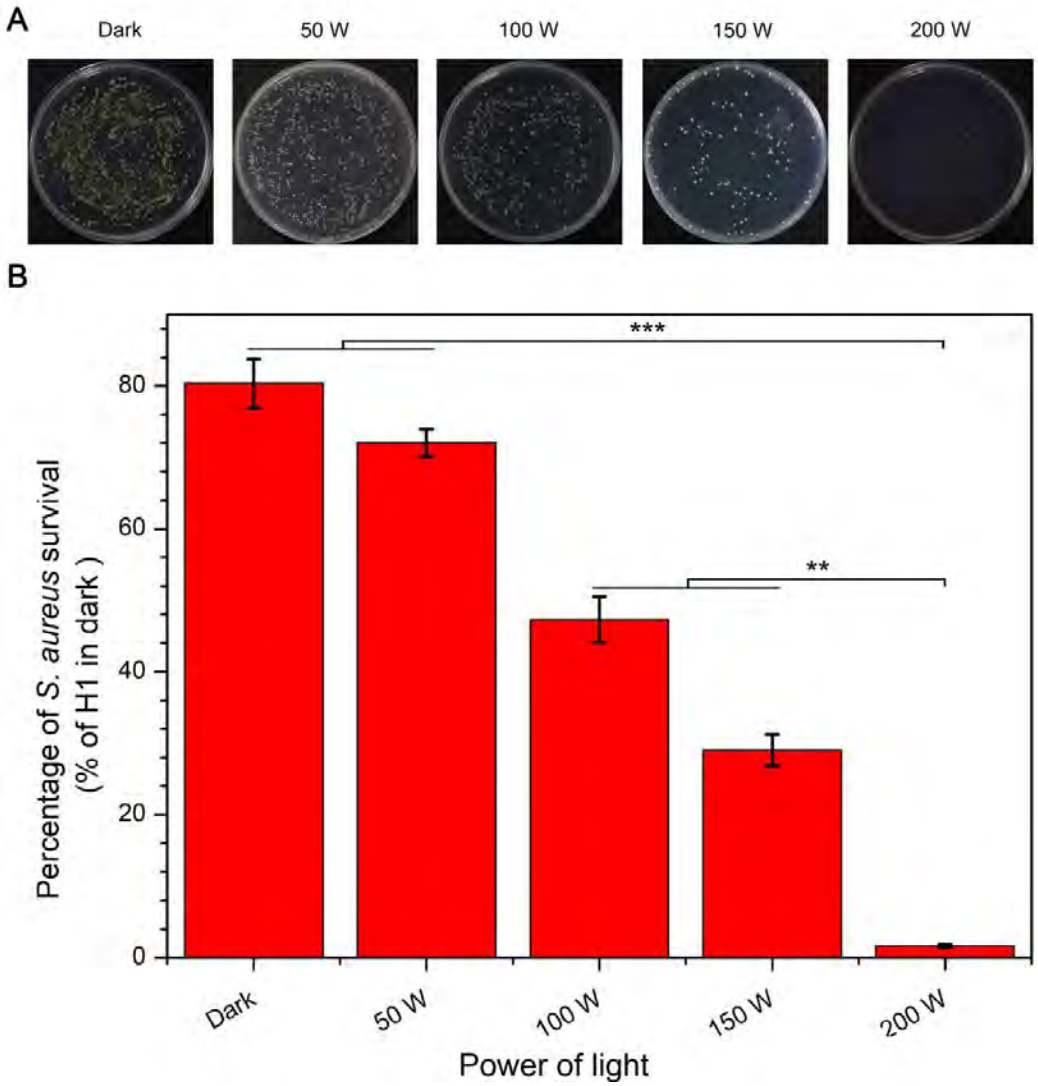

Figure S16. (A) Formed viable colony units of *S. aureus* after exposure to H2 and simulated sunlight with different power for 20 min (with 1 h in darkness); (B) Corresponding survival ratios. The experiment was performed in triplicate and independently (n = 3) with data being mean ± SD.

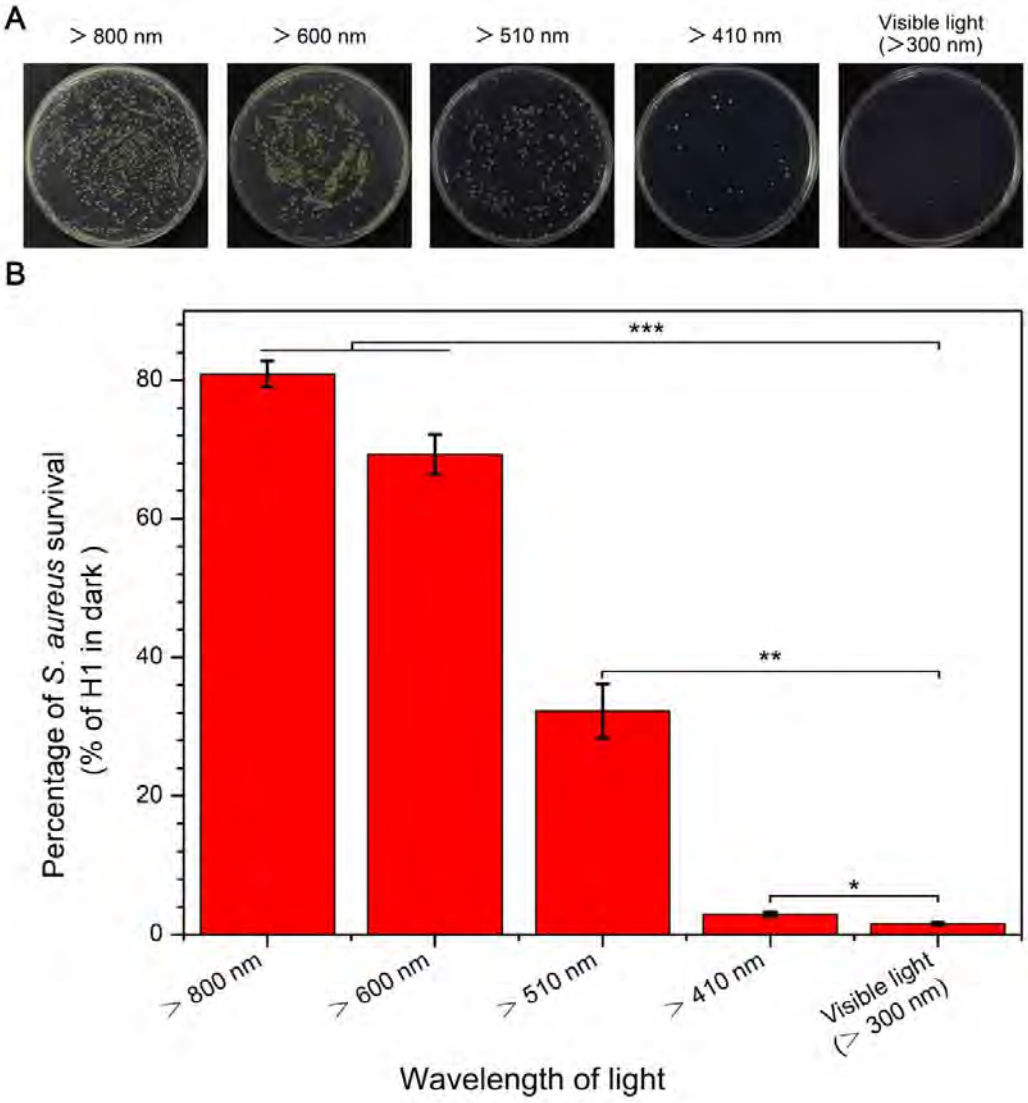

Figure S17. (A) Formed viable colony units of *S. aureus* after exposure to H2 and different wavelengths for 20 min (with 1 h in darkness); (B) Corresponding survival ratios. The experiment was performed in triplicate and independently (n = 3) with data being mean ± SD.

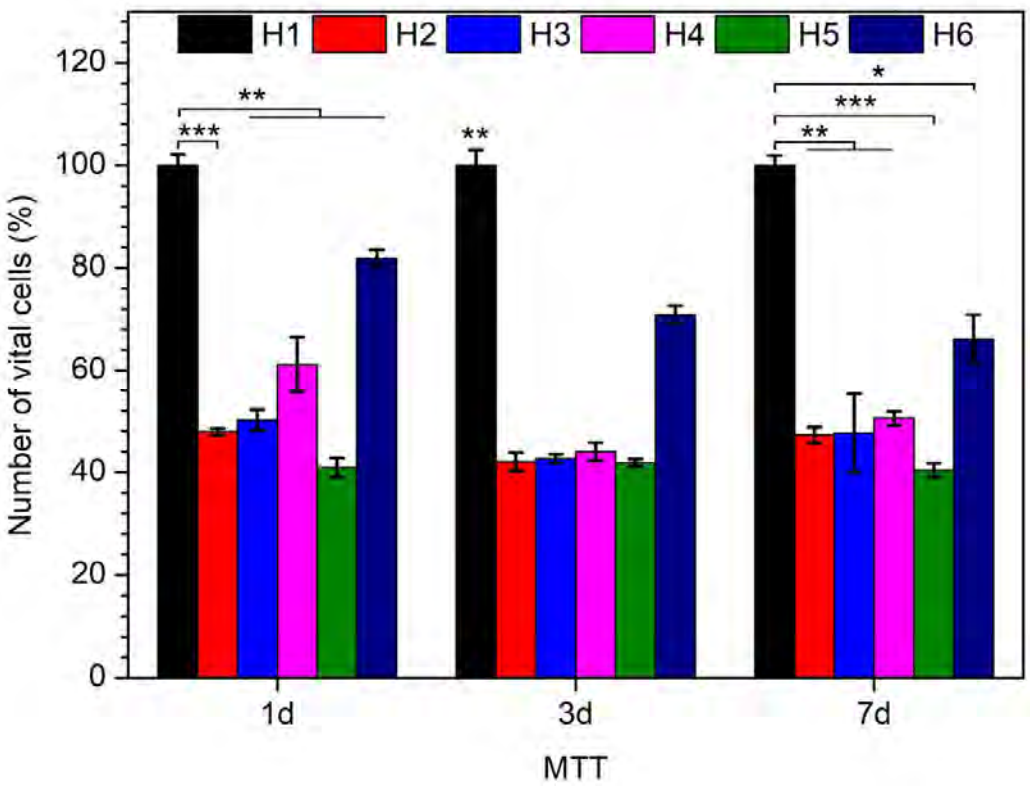

Figure S18. Cell viability treated with the hydrogels at days 1, 3 and 7. The experiment was performed in triplicate and independently (n = 3) with data being mean ± SD.

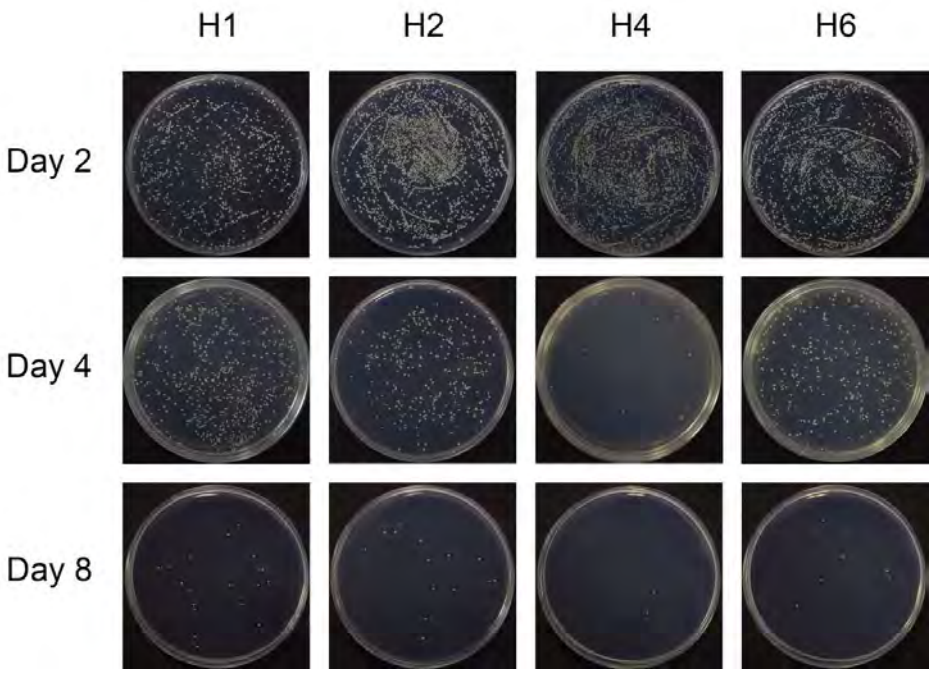

Figure S19. Viable colony units of *S. aureus* formed from the exudate of the wounds at days 2, 4 and 8.

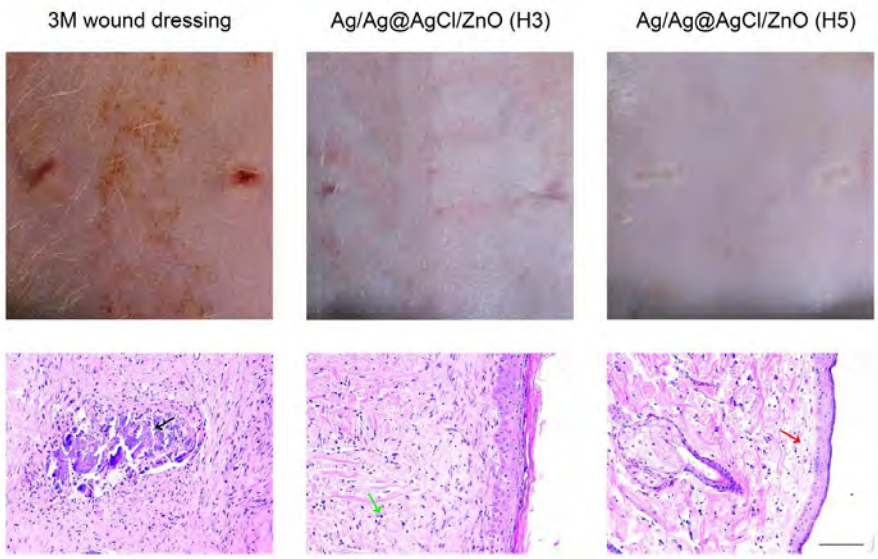

Figure S20. Wound photographs taken from the rats after 14-day treatment by 3M wound dressing, H3, and H5 and the corresponding immunology of histological images of the skin tissue samples on the wounds (Scale bar = 100 μm).

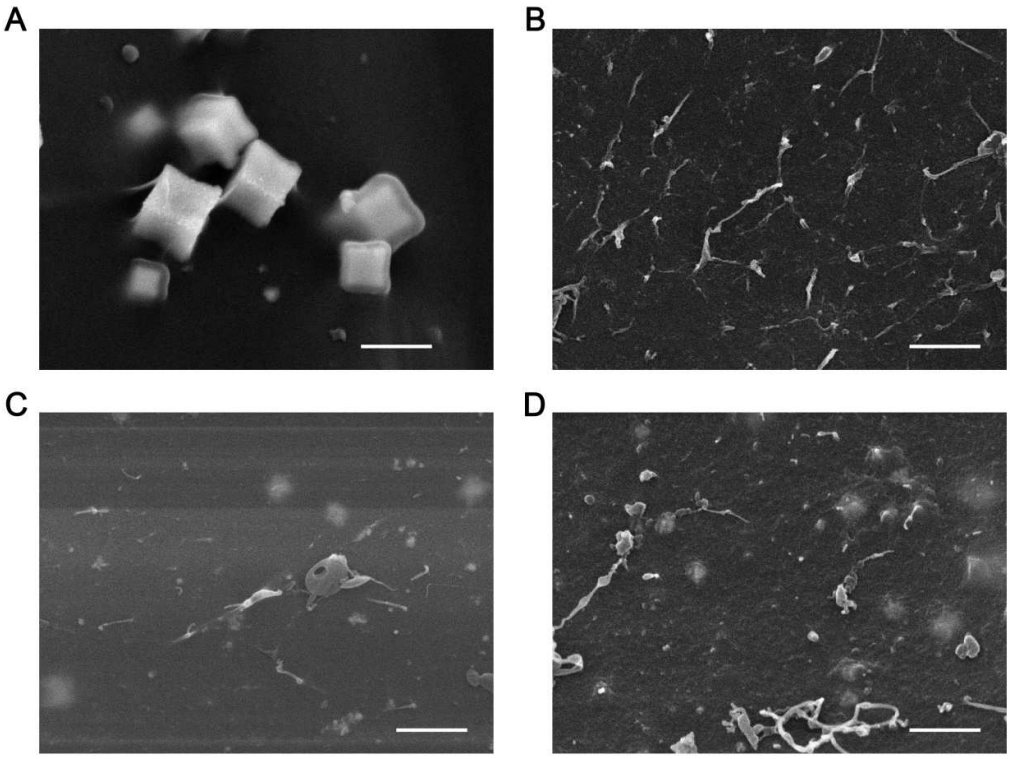

Figure S21. SEM images of (A) Ag/Ag@AgCl nanostructures, (B) H3, (C) H4, and (D) H5 after wound healing in the animal models (Scale bar = 1 μm).

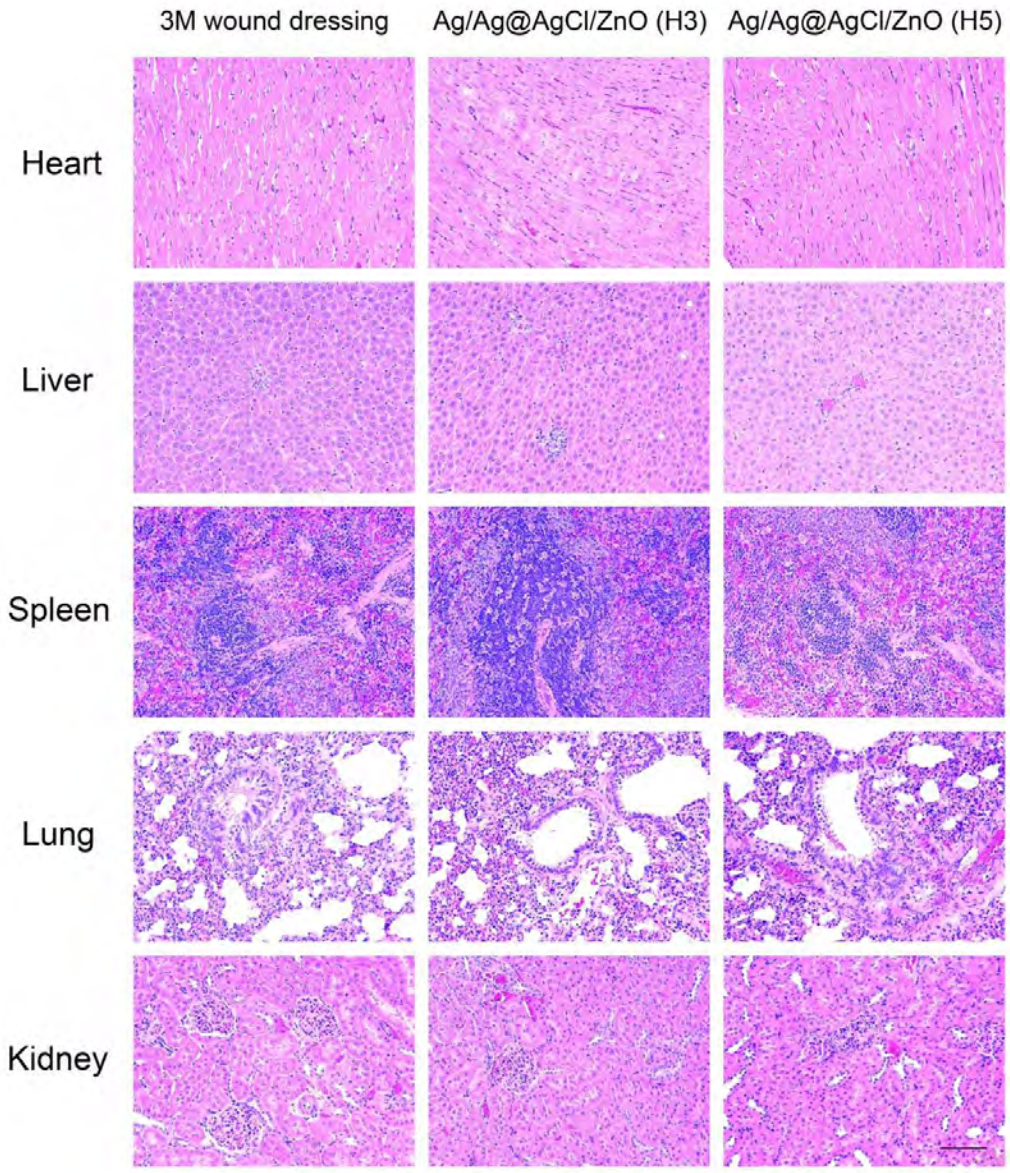

Figure S22. H&E staining of the heart, liver, spleen, lung, and kidney tissue slices after the 14-day treatment for different treatment groups (3M wound dressing, H3, and H5) [Scale bar = 100 μm].

4. References

1. Hu, Y.; Lu, C. H.; Guo, W.; Aleman-Garcia, M. A.; Ren, J.; Willner, I. A Shape Memory Acrylamide/DNA Hydrogel Exhibiting Switchable Dual pH-Responsiveness. *Adv. Funct. Mater.* **2015**, *25*, 6867—6874.

2. Guo, W.; Lu, C. H.; Orbach, R.; Wang, F.; Qi, X. J.; Cecconello, A.; Seliktar, D.; Willner, I. pH-Stimulated DNA Hydrogels Exhibiting Shape-Memory Properties. *Adv. Mater.* **2015**, *27*, 73—78.

3. Ren, J.; Hu, Y.; Lu, C. H.; Guo, W.; Aleman-Garcia, M. A.; Ricci, F.; Willner, I. pH-Responsive and Switchable Triplex-Based DNA Hydrogels. *Chem. Sci.* **2015**, *6*, 4190—4195.